Starshade Technology Development Activity
Milestone 1A:

Demonstration of High Contrast in Monochromatic Light at a Flight-like Fresnel Number

Anthony Harness, N. Jeremy Kasdin, Michael Galvin

Princeton University

Stuart Shaklan, Kunjithapatham Balasubramanian, Victor White, Karl Yee, Richard Muller, Philip Dumont, Simon Vuong, Phillip Willems

Jet Propulsion Laboratory, California Institute of Technology

January 28, 2019

Contents

Executive Summary

We report the results of the first in a series of technology milestone experiments for the Exoplanet Exploration Program Starshade Technology Activity (S5). The goal of this milestone was to demonstrate 10^{-10} instrument contrast at the starshade's inner working angle (IWA) in narrow band visible light. The light source, starshade mask, and camera were configured to represent a sub-scale version of a full scale starshade on orbit. The experiment was executed in the Princeton Starshade Testbed, a 78 m long, 1 m diameter enclosed tube at atmospheric pressure in the basement of the Frick Chemistry building on campus.

The precision-etched silicon starshade mask is actually two starshades, an inner starshade and outer starshade, joined together by narrow radial struts. The two starshades were designed to independently achieve a deep shadow while the struts provide a uniform attenuation. The mask was designed in this way so that the starshade could be supported without using wires or other diffractive structures that would limit the performance to levels well above 10^{-10}. The outer starshade has the additional effect of apodizing the beam to minimize diffraction and reflection contributions from the inner surface of the long tube.

Our experiment achieved better than 10^{-10} contrast over 44% of the circumference of a circle at the IWA, while reaching an average contrast at the IWA of 1.15×10^{-10}. The contrast floor was remarkably low at 2×10^{-11}. Most of the light at the IWA is attributable to a laboratory-scale polarization effect. The physics of light passing through microscopic features limits performance: the narrow gaps between the 1/1000 scale inner starshade petals induce a slight polarization-dependent attenuation and phase shift of the transmitted light. This leads to diffraction lobes appearing between the optical axis and IWA with a peak value of $\sim 7 \times 10^{-10}$. At the IWA, the diffraction lobes are reduced but still exceed 10^{-10} over more than half of the IWA. This is a laboratory scale limitation that will not be present in the flight system where the petal gaps are 1000 times larger and the resulting diffraction is 1 million times fainter than is seen in the laboratory.

Achieving contrast of $< 10^{-10}$ in the region of the starshade unaffected by the (non-flight like) polarization effects results in successful completion of this milestone and demonstrates that both the breakdown of scalar diffraction calculations and the effects introduced by the laboratory are no worse than a contrast of 10^{-10} at the inner working angle and beyond.

1 Introduction

1.1 Background

The Exoplanet Exploration Program (ExEP) has chartered the Starshade Technology Activity, called S5, to develop starshade technology to Technology Readiness Level (TRL) 5 for a future space mission. S5 is focused on optical, mechanical, and formation flying technologies culminating in a series of milestones to be completed between 2019 and 2023.[1] The first three milestones focus on the demonstration of optical performance at flight-required levels:

Milestone 1A: Small-scale starshade mask in the Princeton Testbed demonstrates 1×10^{-10} instrument contrast at the inner working angle (IWA) in narrow band visible light and Fresnel number ≤ 15.

Milestone 1B: Small-scale starshade mask in the Princeton Testbed demonstrates 1×10^{-10} instrument contrast at the inner working angle at multiple wavelengths spanning $\geq 10\%$ bandpass and Fresnel number ≤ 15 at the longest wavelength.

Milestone 2: Small-scale starshade in the Princeton Testbed validates contrast vs. shape model to within 25% accuracy for induced contrast between 10^{-9} and 10^{-8}.

The definition of 'contrast' and the related metric 'suppression' can be found in the S5 technology development plan.[1]

The ability of a starshade to suppress starlight and form a dark shadow depends on its shape. Our design philosophy within S5 has been to divide the issues of starshade shape into two parts: 1) Can we design the right shape for 10^{-10} contrast? And 2) Does the starshade deploy to the right shape? Milestones 1A, 1B, and 2 address only the first question. The successful completion of milestones 1A and 1B will show that the diffraction equations correctly describe the propagation of light between the starshade and the telescope, leading to the formation of a deep shadow. Milestone 2 will then validate the model used to set requirements on the accuracy of the shape such that an imperfect starshade, one that can be assembled, deployed, and maintained throughout the mission, forms a deep shadow. Additional milestones address formation flying, petal shape accuracy, petal positioning accuracy, starshade deployment, thermo-mechanical stability, opacity, and optical edge glint properties.

This report details the experiment and results supporting the completion of Milestone 1A, the initial step in this series of optical performance demonstrations. The experiment was executed in the Princeton Starshade Testbed located on the Princeton campus in the basement of the Frick chemistry building. We describe the experiment configuration, testbed setup, calibration measurements, data collection process, and data analysis approach, resulting in a quantitative measure of the regions around the starshade that meet the milestone. Contrast $< 10^{-10}$ is observed at the IWA, while the average contrast at the IWA is 1.15×10^{-10} with a floor of 2×10^{-11}.

1.2 Mimicking the flight configuration at small scale

The starshade design is driven by two competing factors: it must be far enough in front of the telescope to allow observation of planets in close proximity to their host star and it must generate a dark shadow that is larger than the telescope aperture. Together these

requirements drive starshades to be tens of meters in diameter and tens of thousands of kilometers in front of the telescope. For example, Table 1 shows typical design parameters for the HabEx[2] and Starshade Rendezvous Probe Mission (SRM)[3] mission concepts. The table lists the operational range of the Fresnel number, defined as $N = R^2/(\lambda Z)$, where R is the starshade radius, λ is the wavelength, and Z is the starshade-telescope separation.

	HabEx	SRM	Laboratory
Telescope diameter	4.0 m	2.37 m	5.0 mm
Starshade diameter	52 m	26 m	24.28 mm
Wavelength range	300 - 1000 nm	616 - 800 nm	638 nm
Tel. - starshade sep.	76,600 km	26,000 km	50.0 m
Source - starshade sep.	10 pc	10 pc	27.45 m
Fresnel number	**8.8-29**	**8.1-10.5**	**13**

Table 1: HabEx and SRM Starshade Architectures and Testbed Parameters

For this range of N, the Fresnel approximation is sufficiently accurate to compute the diffraction pattern to contrast levels better than 1×10^{-10}, an assertion borne out by the successful demonstration of a dark shadow in this milestone report. The Fresnel diffraction integral to compute the electric field U at a point p in the telescope pupil plane is given by

$$U(p) \propto \frac{-i}{\lambda Z} \int_0^{2\pi} \int_0^R U_0 e^{\frac{i\pi r^2}{\lambda Z}} r \, dr d\theta \tag{1}$$

$$\propto \frac{-i}{2} \int_0^{2\pi} \int_0^N U_0 e^{i\pi n} \, dn d\theta, \tag{2}$$

where n is the dimensionless quantity $n = r^2/\lambda Z$ spanning the range of Fresnel numbers up to N. When written in the dimensionless form of Equation 2, the equation is independent of R, λ, and Z.

This then brings us to the design of the laboratory experiment, which is greatly reduced in scale yet designed to mimic the diffraction of the flight configuration. Table 1 also gives the parameters of the Princeton starshade testbed. Besides the greatly reduced scale, an important difference between flight and the laboratory experiment is that the light source is only meters away, whereas a star is effectively infinitely far away. For a finite source distance, the effective Fresnel number is the sum of the Fresnel number for the source-starshade distance plus the Fresnel number for the starshade-telescope distance, $N = N_{\text{source}} + N_{\text{tel}}$. The effective distance parameter is $Z_{\text{eff}} = Z_{\text{source}} Z_{\text{tel}}/(Z_{\text{source}} + Z_{\text{tel}})$. For the experiment, we then have $Z_{\text{eff}} = 17.72$ m, resulting in $N = 13.0$. The experiment is then within the operational range for a mission such as HabEx, where $N = 13$ occurs at a wavelength of 680 nm. While the experiment Fresnel number falls outside the operational range of SRM, the integrals overlap for the Fresnel range, n=5.6 to 10.5 (i.e. the petals of the test mask apodize many of the same Fresnel zones as do the petals of SRM). The aperture size of the testbed camera is such that the starshade image is the same number of resolution elements wide in the testbed as for HabEx.

As with a source infinitely far away, the effective distance parameter for a source at a finite distance appears in the kernel of the Fresnel diffraction equation. Consider an incident electric field due to a spherical wave emanating from a distance of Z_0, of the form,

$$U_0(r,\theta) \propto e^{\frac{i\pi r^2}{\lambda Z_0}}. \tag{3}$$

The Fresnel diffraction equation then becomes,

$$\begin{aligned} &\propto \frac{-i}{\lambda Z}\int_0^{2\pi}\int_0^R e^{\frac{i\pi r^2}{\lambda Z_0}} e^{\frac{i\pi r^2}{\lambda Z}} r\, dr d\theta \\ &\propto \frac{-i}{\lambda Z}\int_0^{2\pi}\int_0^R e^{\frac{i\pi r^2}{\lambda}\left(\frac{1}{Z}+\frac{1}{Z_0}\right)} r\, dr d\theta \\ &\propto \frac{-i}{\lambda Z}\int_0^{2\pi}\int_0^R e^{\frac{i\pi r^2}{\lambda Z_{\text{eff}}}} r\, dr d\theta. \end{aligned} \tag{4}$$

The final line of this equation shows that the diffraction at distance Z from a finite-distance source is equivalent to diffraction at distance Z_{eff} from a source at infinity.

The laboratory diffraction pattern is governed by Equation 2, for a value N similar to the values used in flight. We can now appreciate the main point of Milestone 1A: *by showing in the laboratory that high contrast is achieved at flight-like values of N, we show that the full-scale properly shaped starshade will also produce the same level of contrast.*

Still, there are two important differences between the laboratory testing and the flight conditions. The first is due to the geometric scale of the experiment. At the laboratory scale, parts of the starshade pattern have gaps that are only a few times wider than the wavelength of light. Vector diffraction equations are required to determine the resulting polarization-dependent complex amplitude of the light propagating through the gaps. At the flight scale, the smallest gaps are thousands of times wider than the wavelength of light and the vector propagation amplitudes are thousands of times smaller than in the laboratory. Thus the detrimental physics encountered in the experiment is not expected to be present at significant levels at the flight scales. A model of the vector diffraction effects was created to understand the magnitude of the effect and correlate against the measurements seen in the Milestone 1A data. While there is good correlation in the degradation amplitude and location of the vector diffraction, more detailed modeling and correlation with additional data from the upcoming Milestone 1B is needed to have high confidence in the quantitative accuracy of the model.

A second difference between the laboratory testing and flight conditions is the presence of air in the test chamber. Immediately upon closing the chamber, turbulence in the air is seen to degrade the optical performance, so the chambers are allowed to settle for a few days before collecting data, by which time turbulent effects are no longer seen. The Rayleigh scattering from the atmospheric molecules provides a diffuse background noise which affects both the overall suppression and the localized contrast. Similar to the vector diffraction, this non-flight phenomenon was modeled in a coarse way to understand the magnitude of the effect and correlate to the observations in Milestone 1A. An independent review of the model and additional data from the upcoming broad band measurements is needed to provide sufficient confidence in the analytical prediction of the effect in order to subtract it from the

testbed measurement data and provide potentially a more realistic flight-like performance prediction.

Therefore *the numerical results of Milestone 1A provided in this report do not take into account or remove the analytically predicted effects of vector diffraction or Rayleigh scattering.* Even with these effects and the degraded performance of a portion of the region at the IWA, contrast levels $< 10^{-10}$ are still clearly observed in the unaffected regions, with a diffraction floor of $\sim 2 \times 10^{-11}$. We anticipate being able to address these non-flight conditions more extensively in the revision of this report which incorporates the broad band measurements for Milestone 1B.

1.3 Prior experiments

A number of starshade laboratory and field experiments have been reported in the literature, with separations ranging from 13 m to 4 km, and Fresnel numbers ranging from 8 to 600.

In 2007, Leviton et al.[4] reported a deep suppression level of 2.5×10^{-7} in broadband sunlight at $N = 33$ ($\lambda_{\rm center}$=450 nm, $Z_{\rm eff}$ =10.4 m, r =12.5 mm) using a wire-suspended, etched silicon wafer in a 42 m long testbed. The performance was partially limited by glint from the wire suspension system, and partially by the quality of the mask, particularly the micron-scale petal tips. Samuele et al.[5,6] also used a wire-suspended starshade with a collimated beam in a 43 m long tube to achieve 6×10^{-7} contrast at a flight-like Fresnel value $N = 13$.

In a much larger, outdoor experiment, Glassman et al.[7,8] used a 50 cm diameter starshade held by a post and placed in the middle of a 2 km path between a broadband LED source and a small telescope on a dry lakebed. Limited by atmospheric turbulence, dust, and reflection from the desert floor, the light source was suppressed by $\approx 1 \times 10^{-6}$, but they nonetheless demonstrated 7×10^{-10} contrast near the edge of the starshade. At a Fresnel number of $N \approx 250$, the suppressed light was highly localized near the edges of the starshade such that a few resolution elements away from the edge, the contrast was orders of magnitude deeper than the overall suppression level.

With a flight-like geometry at $N \approx 12$, Harness et al.[9,10] used the auxiliary feeds of the McMath Solar Telescope at Kitt Peak to direct starlight to a 24 cm diameter post-mounted starshade observed from a telescope on a ridge 2.4 km away. The experiment reached a contrast level of 3×10^{-5}, limited by the quality of the McMath optics and atmospheric turbulence, and is the only set of observations to date using real starlight with a starshade.

In all of the aforementioned experiments, the starshade was supported either by wires or by a support post. In 2009, Cady et al.[11] described an approach that used a ring of petals, essentially an "outer starshade" to suspend the inner starshade. The outer starshade held the inner one in place while also controlling beam diffraction that would be dominant with a circular structure. The experiments achieved suppression levels[12] of $< 4 \times 10^{-7}$ and contrast of 4×10^{-10} between petals, but at a Fresnel number of $N = 580$. This is equivalent to having a large starshade on orbit with an inner working angle of 400 milli-arcsec.

The point of the current milestone is to achieve flight-like contrast levels with a flight-like Fresnel number and flight-like observational configuration, scaled to fit into a laboratory setting.

2 Experiment Design

2.1 Testbed configuration

The design of the experiment is simple: image a light source from within the deep shadow created by a starshade and measure the efficiency with which the starshade suppresses the on-axis light. The testbed consists of three stations containing a laser, starshade, and camera. A schematic of the testbed with size scales can be found in Figure 1 and Table 1. Distances between components within the three stations were measured to < 1 cm accuracy with a surveyor's station. The beam line is contained in 1 m diameter steel tubing (at atmospheric pressure) to seal the testbed from stray light and dust and to help stabilize the atmosphere. The tube is wrapped in fiberglass insulation (Figure 2) to minimize thermal changes caused by the external HVAC system. Opening any of the testbed stations disturbs the atmosphere inside the tube, adding air turbulence to the beam path and stirring up dust. To minimize how often the testbed is opened, all equipment is built to be remotely operated. Further details of the testbed design can be found in Refs. 13, 14.

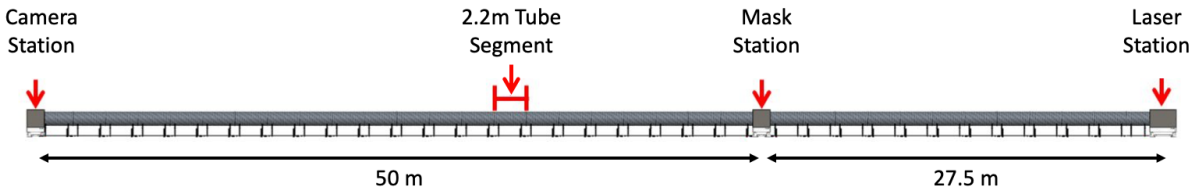

Figure 1: Layout of testbed showing distances between camera, starshade, and laser stations.

Figure 2: Standing at the camera station and looking down the length of the testbed toward the mask and laser stations. The white insulation minimizes the effects of external temperature fluctuations.

2.2 Light source

The light source serving as the artificial star is a 20 mW, multi-channel laser diode operating at 638 nm. To minimize heat sources in the enclosure, the laser is located outside and fed in via a polarization-maintaining single-mode fiber optic. Shown in Figure 3, the fiber terminates with a collimator and is focused by an objective lens through a 100 μm pinhole to filter out high-order aberrations. The filtered gaussian beam has a FWHM of 28.7 cm by the time it reaches the starshade, with an amplitude sag across the 12.1 mm radius of the inner starshade of 0.5% and across the full 25 mm radius of the outer mask of 2.1%.

The polarization state out of the fiber is measured by monitoring the variation of the output power as the light is passed through a quarter-wave plate and linear polarizer while varying the fast axis of the quarter-wave plate. Following the analysis outlined in Ref. 15, the Stokes parameters are derived from a fit of Fourier coefficients to the data. The fit to the data is shown in Figure 4a, with the resultant polarization ellipse shown in Figure 4b.

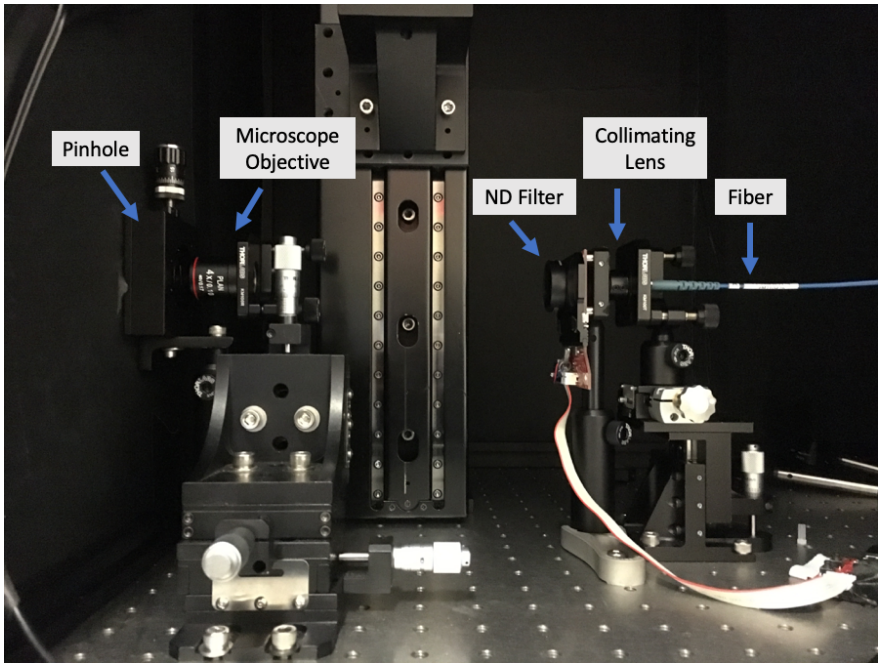

Figure 3: Fiber-fed laser and spatial filter assembly at the light source station.

2.3 Starshade design

The starshade mask consists of an inner starshade representative of a free floating occulter that is supported in a silicon wafer via radial struts. The outer ring of the support wafer is also apodized to minimize diffraction. Both apodization profiles are designed independent of each other using the numerical optimization scheme outlined in Ref. 16. We impose a constraint on the radius of the inner starshade to have Fresnel number < 15 and constrain the valleys between the starshade petals to have widths > 16 μm to minimize non-scalar diffraction that can arise when propagating through features comparable to the size of the

wavelength of light. The combined, radial apodization profile is shown in Figure 5a. This profile is multiplied by 0.9 to provide width to the radial struts and petalized into the starshade shape shown in Figure 5b. The manufactured mask is shown in Figure 6a.

2.4 Starshade mask manufacturing

The starshade mask is etched into a silicon-on-insulator (SOI) wafer via a Deep Reactive Ion etching process and coated with a thin layer of gold to maintain opacity. The allowed tolerances on the shape are very small, ~ 100 nm, and have thus far been the limiting factor in achieving 10^{-10} contrast. Previous iterations using contact lithography were limited by a global over-etching of the mask pattern of > 400 nm, which limited the achievable suppression to $> 4 \times 10^{-8}$. Switching to a direct write electron beam lithography process and biasing the design helped to minimize the over-etch to < 30 nm. The SOI device layer is made as thin as is practical (2 μm) to minimize non-scalar effects as light propagates through the narrow valleys between petals. A schematic cross-section of the wafer is shown in Figure 6b and more details on the manufacturing process can be found in Refs. 17, 18.

2.5 Calibration mask

A circular aperture mask is used to calibrate the throughput of the system and to convert measurements of the occulted light source to a contrast value. This mask is etched out of a 500 μm thick silicon wafer via a Deep Reactive Ion etching process. The radius of the mask is set to equal that of the outer apodization profile to maintain consistency in the size of the limiting aperture.

2.6 Mask holder

During an observation run, we use a mechanized mask changer to take measurements using both the starshade and calibration masks while keeping the testbed sealed. The mask changer, shown in Figure 7a, uses a planetary gear to cycle between masks. Each revolution of the planetary gear changes the orientation of the mask and allows us to identify defects on the mask. The mask changer is attached to a baffle wall (see Figure 7b) such that the only light able to propagate downstream goes through the mask. Measurements have shown that light leakage through a circuitous path through the mask changer is negligible in our experiments.

2.7 Telescope optics

Contrast measurements are made with the camera focused to the plane of the light source, simulating an exoplanet observation. Suppression measurements are made while focused on the entrance pupil of the telescope, mapping the intensity of the diffraction pattern in the starshade's shadow. The telescope is remotely aligned in the shadow by centering on the diffraction pattern. Our optics system has pupil (suppression/alignment) and far field (contrast) imaging modes that can be remotely toggled.

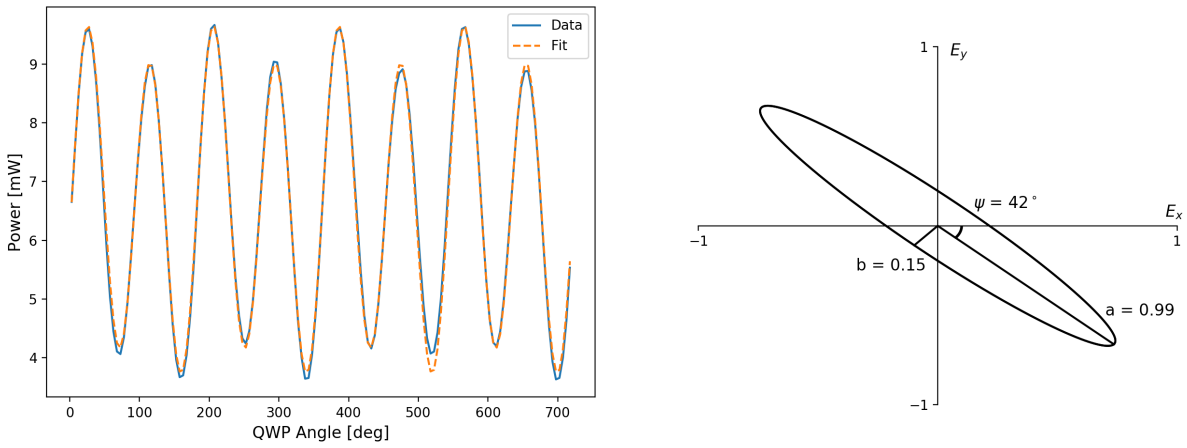

(a) (b)

Figure 4: (a) Laser power vs. quarter-wave plate angle as light is passed through a rotating quarter-wave plate and stationary linear polarizer. (b) Resultant polarization ellipse, with axes aligned with the camera. The polarization fraction is 96%

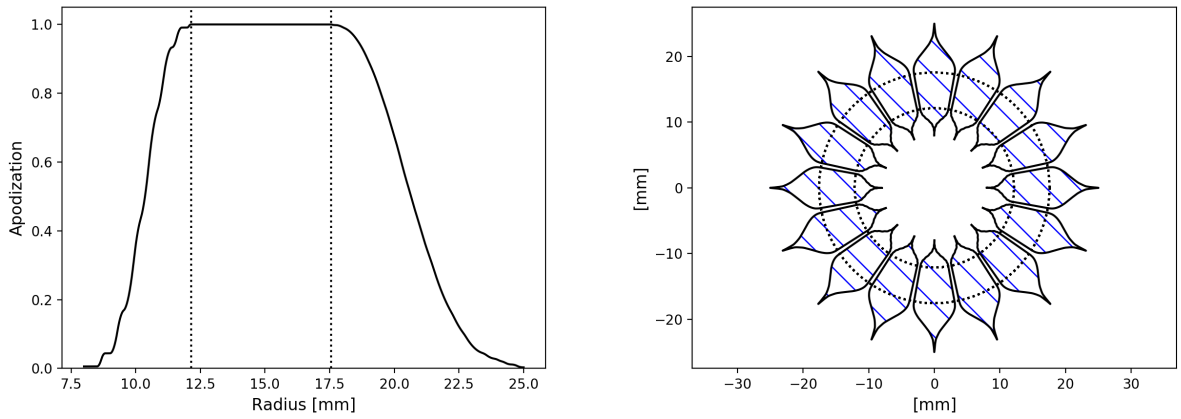

(a) (b)

Figure 5: (a) Apodization (0 = opaque, 1 = transparent) as a function of radius. (b) Blue-striped regions are transparent and white regions are opaque. The dotted lines denote the inner and outer working angles, between which the apodization is at its peak value.

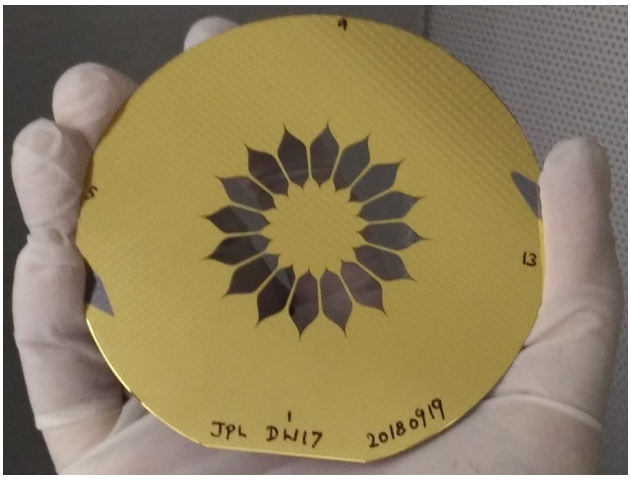

(a)

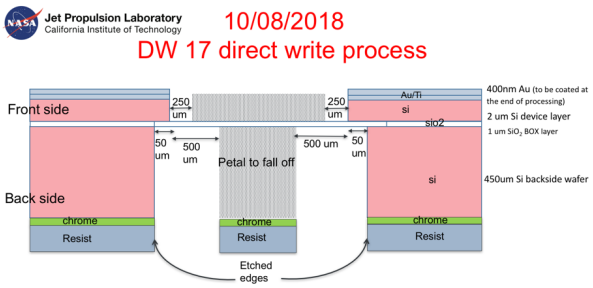

(b)

Figure 6: (a) Starshade mask etched in SOI wafer, manufactured at MDL. (b) Cross section schematic of mask. The optical edge is defined by the 2 μm thick Si device layer.

(a)

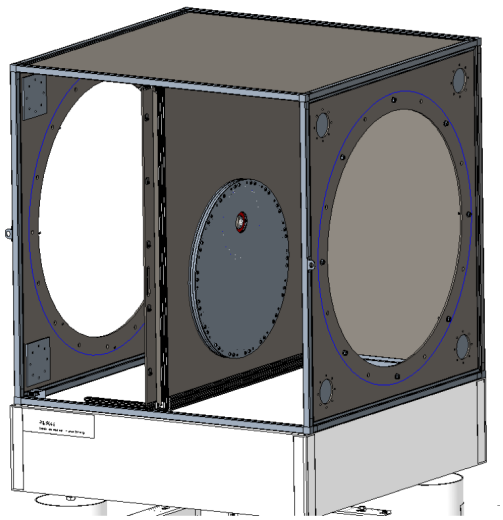

(b)

Figure 7: (a) The sun gear of the mask changer is driven by a stepper motor, which rotates the planetary gears holding the starshade and calibration masks. (b) CAD schematic of the mask holder installed into the baffle wall of the mask station.

A schematic of the optical system is shown in Figure 8 and its properties are presented in Table 2. Farthest upstream is a filter wheel with various sized apertures that provide larger fields of view of the diffraction pattern during alignment. L1 and L2 are fixed, while L3 toggles into alignment during pupil imaging mode. Figure 9 shows a photo of the camera + telescope optics (contained in light-tight box) mounted to a translation stage in the camera station.

Parameter	Value
Aperture diameter	5 mm
Focal length	500 mm
PSF FWHM	27 arcseconds
Active pixels	1024×1024
Pixel size	13×13 μm
Pixel resolution	5.4 arcseconds/pixel
Pupil mode resolution	23 μm/pixel

Table 2: Telescope / camera parameters

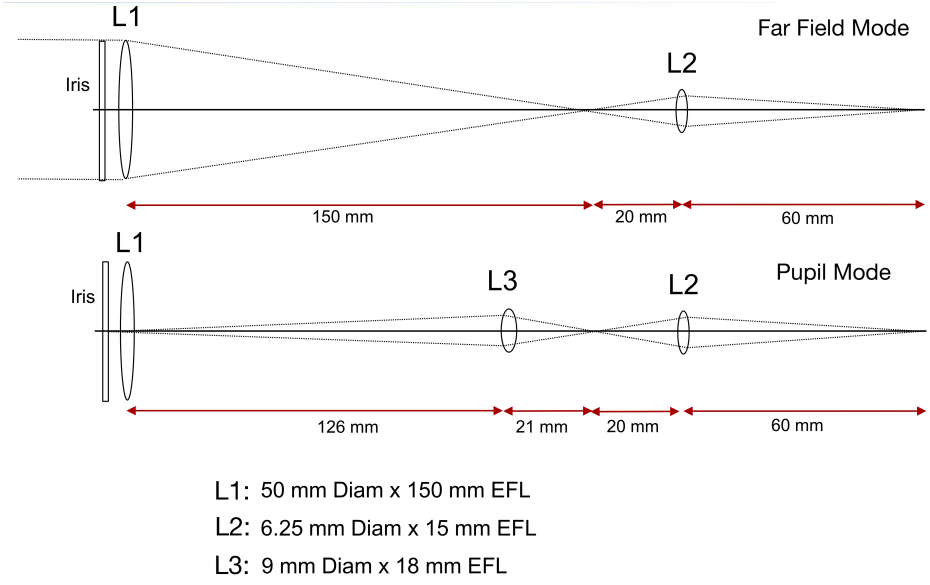

Figure 8: Lens diagram of telescope system. L3 toggles in/out of the beam line to switch between far field imaging (top) and pupil imaging (bottom) modes.

2.8 Detector

The camera is an Andor iXon Ultra 888 EMCCD. For better noise performance at our high photon count rates, we operate the camera with its conventional amplifier, i.e., not

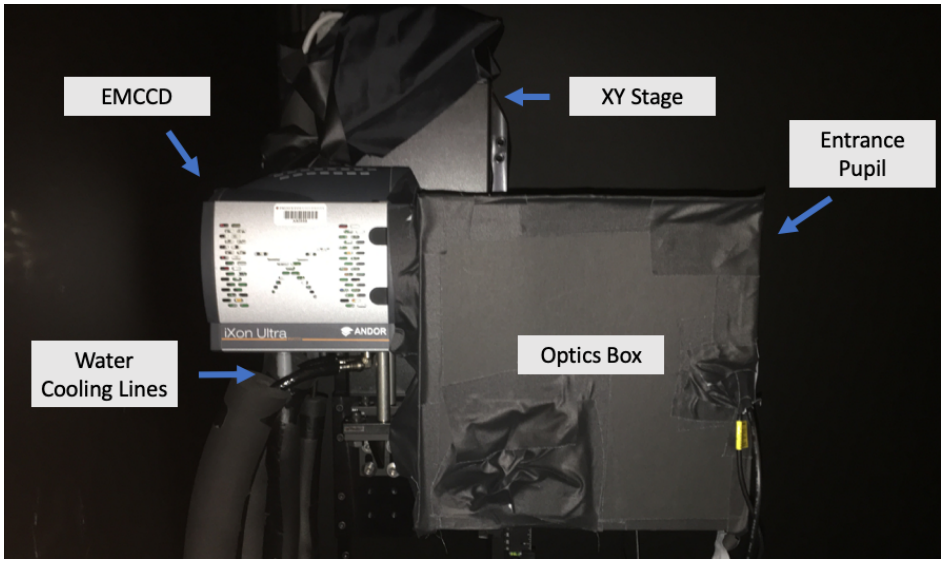

Figure 9: Camera + telescope optics mounted to a 2-axis translation stage in the camera station. The telescope optics are contained in the black, light-tight box.

electron-multiplying. The camera is liquid cooled down to -90°C to eliminate most of the dark current and we estimate the read noise in Section 4.1.2. The dominant noise source in our observations is shot noise from the source itself.

3 Optical Models

3.1 Scalar diffraction model

The size scales and distances involved in the starshade architecture employ the assumption that the propagation of light past a starshade can be fully described by scalar diffraction equations. This assumption has been made since starshades' inception and is made in the design of the apodization function describing the starshade shape; demonstration of its validity is the driving motivation for these small scale starshade experiments. Under this assumption, the governing equations depend solely on the Fresnel number.

A number of modeling codes have been developed to efficiently solve the diffraction equations over the large range in size scales involved in the starshade architecture. These codes generally exist in two families: those that use a Green's theorem approach to turn the two-dimensional diffraction integral into a one-dimensional line integral around the edge of a binary occulter;[19–21] and those that perform a standard Fresnel propagation on a two-dimensional grid approximating a binary mask.[21,22] These codes have been shown to be in agreement and we do not distinguish between them in this report.[21]

3.2 Vector diffraction model

Initial experiments conducted in this testbed showed good agreement between the experimental data and a scalar diffraction model.[23] In these tests, the starshade performance was limited to a suppression of 4×10^{-8} due to a global over-etching of the starshade shape during the manufacturing process. Improvements in manufacturing eliminated the over-etching and we were able to reach lower suppression levels, at which point the scalar model diverged from the experimental data as it predicted a much lower suppression than observed.[24] These results led us to incorporate the effects of non-scalar diffraction into our optical model and this brought the models back into agreement with the data. Detailed in Ref. 24 and still under development, the vector diffraction model uses a Finite Difference Time Domain (FDTD) solution to Maxwell's equations[25] to simulate the propagation of light through the narrow gaps between the petals of the starshade. The output of the FDTD code provides a phase and amplitude change, dependent on the mask material and thickness, that can be applied to the scalar model. This model provides much better agreement to experimental data and can account for the polarization-dependent signatures observed in the data, but still needs refinement to match the observed data to high precision.

4 Experiment Calibration Data

The following sections detail the calibration of equipment and the estimation of the values and uncertainties of parameters entering the contrast definition provided in Appendix A. Our uncertainty is dominated by systematics, most dominantly the free space correction and the neutral density filter calibration, which do not benefit from averaging over additional images or pixels. Detailed individually in the following sections, we estimate a total 1σ systematic error of 2.3%.

4.1 Detector linearity

4.1.1 Gain

The inverse-gain of the camera (in units [electrons/count]) is estimated from the noise properties of flat field images. A series of flats are taken with varying exposure times to span pixel counts across the full well depth of the detector. At each exposure time, the variance of a difference image is used to estimate the photon noise associated with that image. Figure 10 shows the variance in electrons as a function of mean value in counts. The slope of this line is the inverse-gain in units of e^-/ct. We measure $G = 0.768$, where the manufacturer quotes the inverse-gain to be 0.790. From Figure 10, we can see the detector's response remains linear up to 54,000 counts, after which the full well of the pixel saturates.

4.1.2 Image noise estimation

The dominant contributions to the uncertainty in counts collected during each exposure (s_u, s_m) are: photon noise from the source, background light, and detector dark noise and read noise. We can ignore noise from clock induced charge in the detector electronics, as

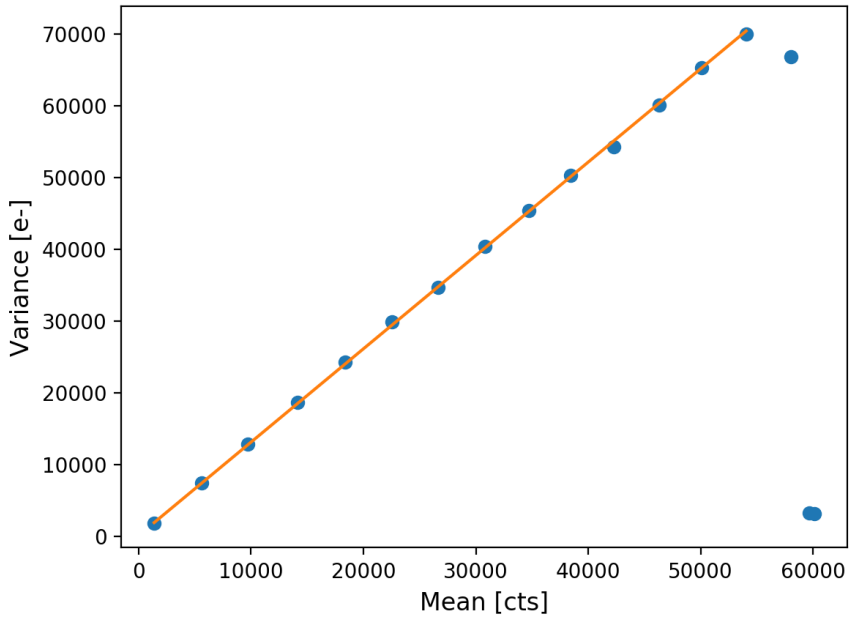

Figure 10: Data taken from flat field images of varying exposure time. The variance of the image (y-axis) is plotted against the mean number of counts (x-axis). The slope of this line is the inverse-gain of the detector in units of electrons/count.

this is estimated to be $< 3 \times 10^{-3}$ events/pixel. Read noise is estimated from the variance of a difference of 2 bias frames of 10 μs exposure times to be $\sigma_R = 3.20$ e$^-$/pixel/frame. We combine the number of counts from background light and detector dark noise into the variable d, which is estimated from dark exposures taken with an equal exposure time. The uncertainty in the measurement of s counts in a single image j is given by

$$\sigma_{s_j}^2 = \frac{s_j}{G} + 2\sigma_d^2 + \sigma_R^2. \tag{5}$$

For each observation mode, a number (n_{frames}) of images are taken and median-combined into a master image. Taking the median value helps to eliminate outliers such as cosmic ray hits. For simplicity, we propagate the uncertainty of the mean and acknowledge that this is a conservative estimate as the uncertainty of the median will be less than that of the mean. The variance in s counts obtained from n_{frames} frames is given by

$$\sigma_s^2 = \frac{\sigma_{s_j}^2}{n_{\text{frames}}} \tag{6}$$

4.1.3 Linearity

We estimate the detector linearity by imaging a constant brightness source at varying exposure times and examining the detector response. Deviations from linearity estimated here

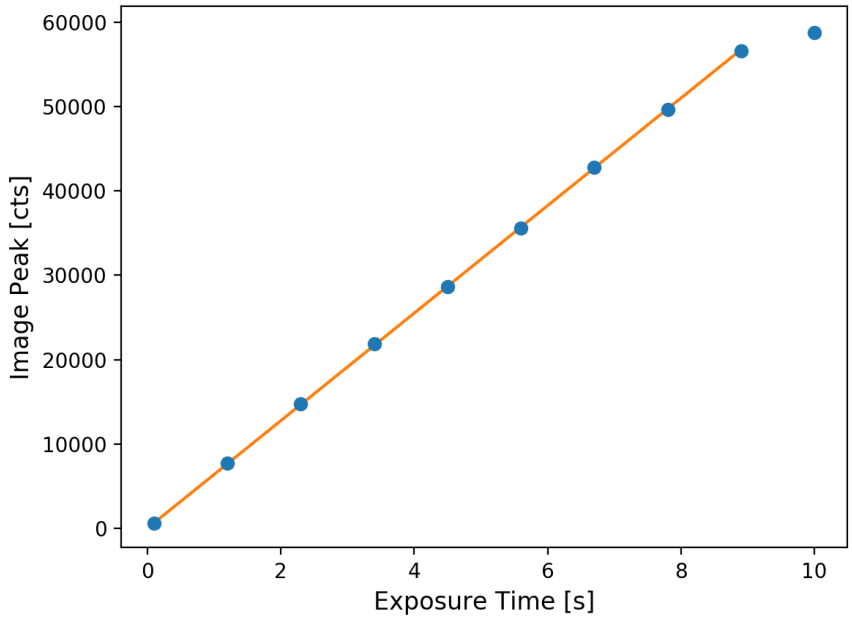

Figure 11: The PSF peak as a function of exposure time while imaging a constant brightness laser through the calibration mask.

are propagated into our uncertainty calculation with the variable Q, representing the quantum efficiency of the detector. In Figure 11, we plot the PSF peak as a function of exposure time and fit a linear line to the response. From these results, we give the uncertainty in the detector linearity a conservative estimate of 0.3%, 1σ.

4.2 Focal length

The focal length is calibrated by imaging two LEDs located at the source end and comparing the image distance to the known separation and distance of the LEDs. From this we calculate the focal length to be 500 ± 10 mm.

4.3 Laser power stability

We measure the long term stability of the laser power with a photometer measuring the light exiting the pinhole over a period of 40 hours. These data are shown in Figure 12. There is a steady decrease in power over time, with a $< 1\%$ decrease over 40 hours. Since a contrast observation run takes less than 12 hours, we estimate the 1σ uncertainty in the laser power to be 0.15%.

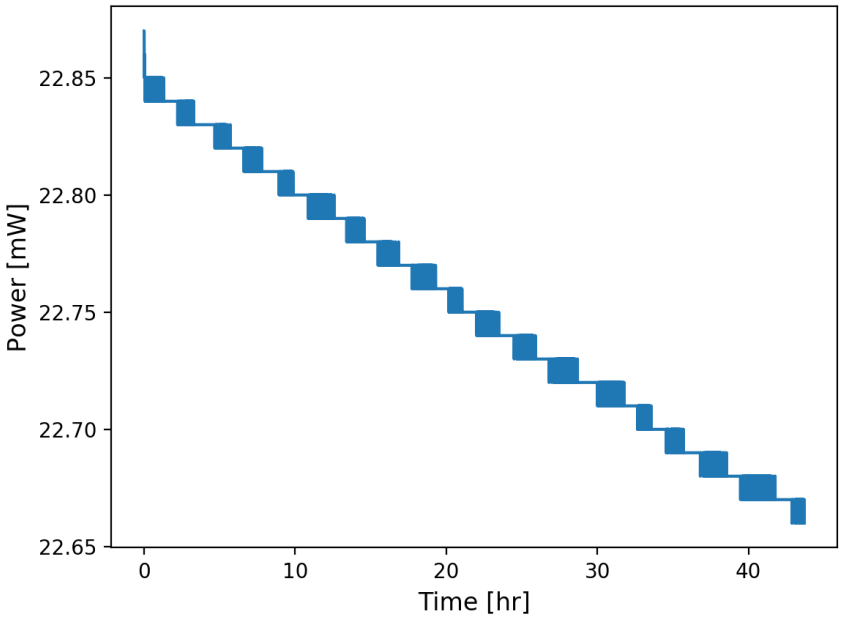

Figure 12: Laser power measured at the spatial filter pinhole over a period of 40 hours. 1 mW steps are power meter quantization.

4.4 Atmosphere transmission

During the science observations, we record the laser power with a photometer at the mask station to estimate any change in brightness due to variations in the transmission of the atmosphere (ε). Using the data in Figure 13 and taking into account the variance from the laser power itself, we estimate σ_ε to be at most 1%.

4.5 Neutral density filter

A neutral density filter is used during unocculted measurements in order to span the 10 orders of magnitude difference between occulted and unocculted. The filter is mounted to a translation stage that toggles in and out of place remotely. The quoted optical density of the filter used is $OD = 7$, where the transmission factor of the filter is $\nu = 10^{-OD}$. We calculate the true transmission factor by using a photometer to measure light exiting the pinhole with (P_{in}) and without (P_{out}) the filter in place. This process is repeated multiple times and we find this measurement is very repeatable. We measure the transmission factor to be

$$\nu = \frac{P_{in}}{P_{out}} = \frac{1.09 \text{ nW}}{13.58 \text{ mW}} = 8.03 \times 10^{-8} \tag{7}$$

This measurement is within the limits specified by the filter manufacturer, but also accounts for a decrease in power that can occur when the focus of the spatial filter is slightly

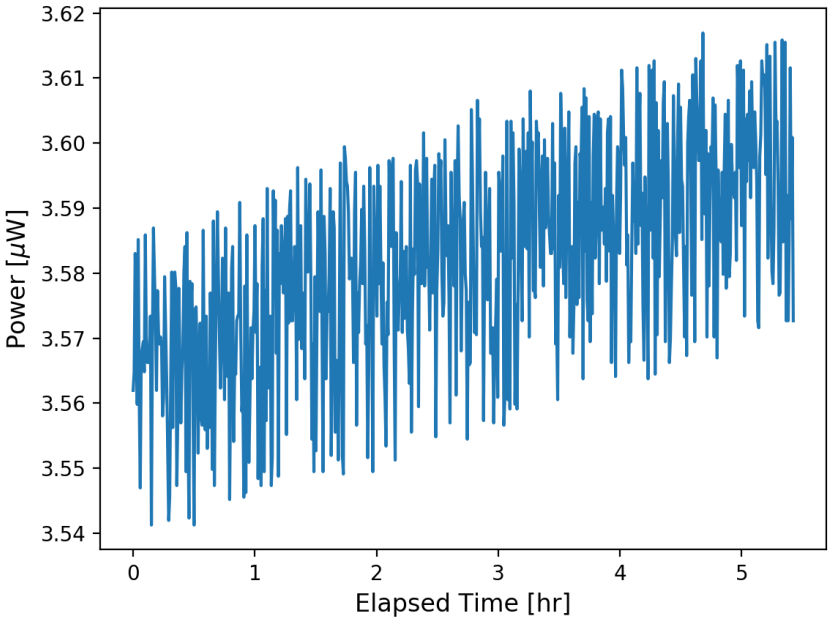

Figure 13: Laser power measured at the mask station during Run 1 science observations.

moved off the pinhole when the filter is put in place. We propagate the photometer's quoted measurement uncertainty of 0.5% and resolution of 10 pW to estimate $\sigma_\nu/\nu = 1\%$.

We recalibrate the filter after the observation runs and measure the transmission factor to be 7.97×10^{-8}, within our uncertainty.

4.6 Free space calibration correction

As detailed in Appendix A, to tie the contrast measurement to the space-based case, we must account for the difference in light propagating through the finite aperture of the calibration mask and that of free space propagation. We use a diffraction model to estimate the value and uncertainty in the parameter γ. If intensity in the focal plane is given by I, we define the free space correction as,

$$\gamma = \frac{max\left\{I_{\text{free space}}\right\}}{max\left\{I_{\text{calibration mask}}\right\}}. \tag{8}$$

Using the scalar diffraction model described in Section 3.1 and given the distances measured in the lab, we generate an image of a 50 mm diameter circular aperture and compare that to an image of free space propagation of a spherical wave to calculate γ. There is uncertainty in the size of the calibration mask that could change the value of γ (it is only weakly dependent on distance). Figure 14 shows γ as a function of circle radius illustrating its highly oscillatory nature. We can, however, leverage measurements of the diffraction pattern to constrain the radius.

Figure 15 shows a slice across the pupil image of the calibration mask. We use an analytic

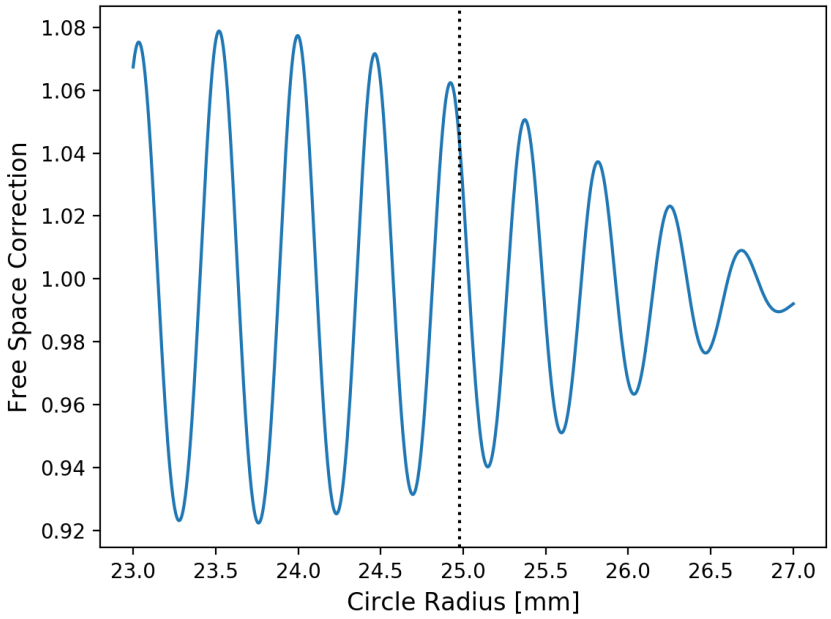

Figure 14: Modeled free space correction (γ) as a function of calibration mask radius. The vertical line denotes the radius of the best fit model to the diffraction pattern in Figure 15.

model of scalar diffraction through a circular aperture to find the best fit model to the data. We find a radius of 24.98 mm fits the data best and that, as evidenced by the oscillatory nature of Figure 14, the diffraction pattern allows us to rule out radii where the free space correction < 1. Figure 15 shows the a cross-section of the pupil image with models of the best fit radius (24.98 mm) and a radius (25.15 mm) in which the center of the diffraction pattern is a null, rather than a peak. The shape of diffraction pattern is quickly changing with radius and we can easily rule out radii outside of the range $r \in [24.85\text{mm}, 25\text{mm}]$. Our best fit radius of 24.98 mm gives a free space correction of $\gamma = 1.04$. Taking the maximum deviation from 1.04 within our allowed radii range, we conservatively estimate the 1σ uncertainty in γ to be 2%.

5 Experiment Contrast Data

The data collection procedure is summarized in Appendix B and a summary of the observation runs is presented in Table 3. We performed three runs with the mask rotated at clocking angles 0°, 120°, 240° and a second run at 0° to check for any change over a week timespan. Exposure times were chosen to have a peak flux level of $\sim$ 46000 counts, well within the linear region of the detector. A median combined raw (not background subtracted) science and calibration image for Run 1 is shown in Figure 16. Histograms of the counts in a typical background image (for the short calibration observations and the longer science observations) are presented in Figure 17. Even for the 20 minute exposures, cooling the camera to -90°C

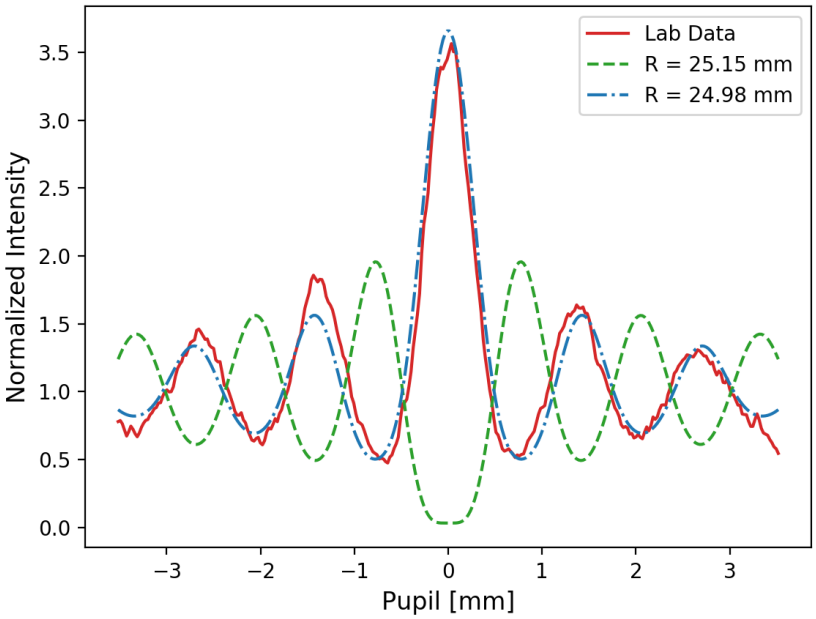

Figure 15: Slice across pupil image of the calibration mask. Lab data are in red, a model with circular mask of radius 24.98 mm and 25.15 mm is in blue-dashed and green, respectively.

effectively eliminates all of the detector dark noise.

Observation Run	Date	Mask Angle	Science Exposure Time	Calibration Exposure Time
1	1/1/19	0°	1200 s	7 s
2	1/5/19	120°	1200 s	7 s
3	1/6/19	240°	1200 s	7 s
4	1/7/19	0°	1200 s	7 s

Table 3: Summary of contrast observations.

Science and calibration images are background subtracted and median combined into master images. The peak unocculted value is taken as the peak value in the master calibration image. The contrast map is generated by applying Equation 13 in Appendix A to the master science image.

Figure 18 shows the contrast map with overlaid starshade shape for Run 1 and Figure 19 compares the contrast maps for all 4 observation runs. Immediately obvious are the bright lobes located at the inner valleys between the petals that are aligned with the polarization direction and remain so when the mask is rotated 240° in Run 3. Comparison to the vector diffraction model in Section 6 shows this is well explained by non-scalar diffraction.

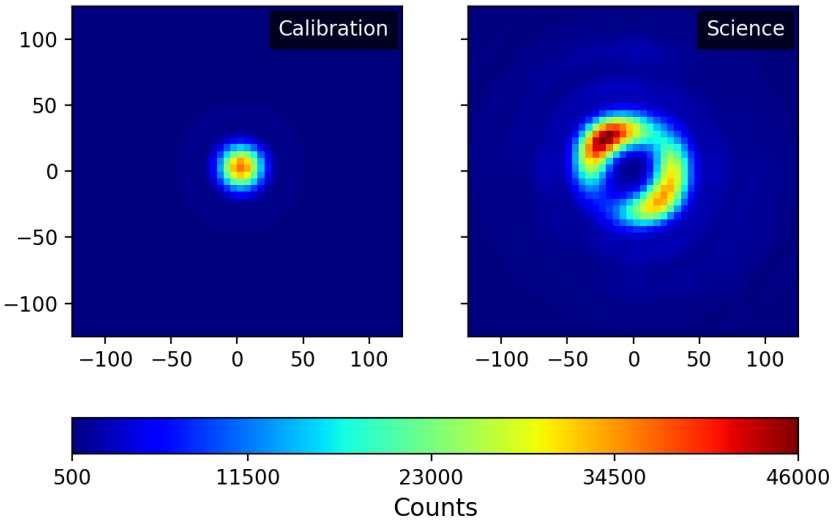

Figure 16: Median-combined calibration (left) and science (right) raw images for Run 1.

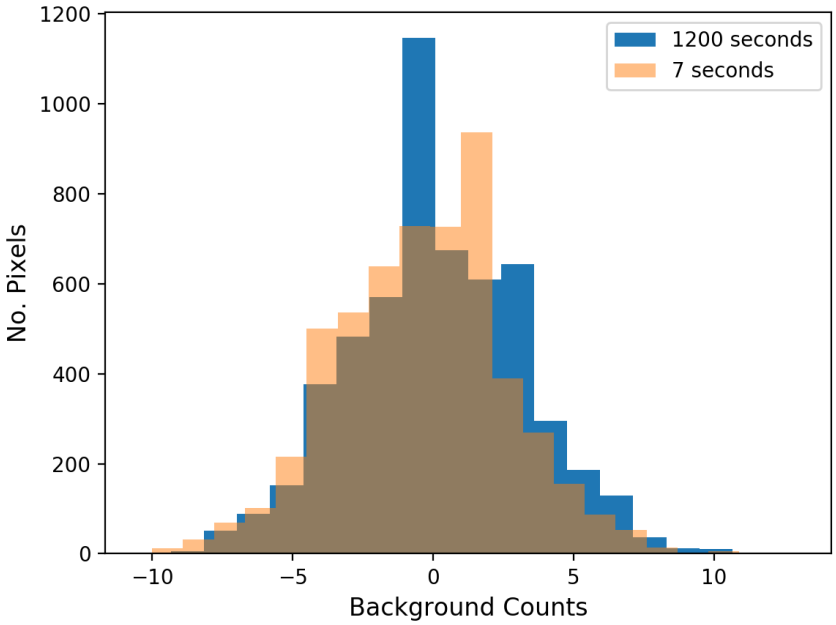

Figure 17: Histogram of background counts for science (1200 s) and calibration (7 s) observations.

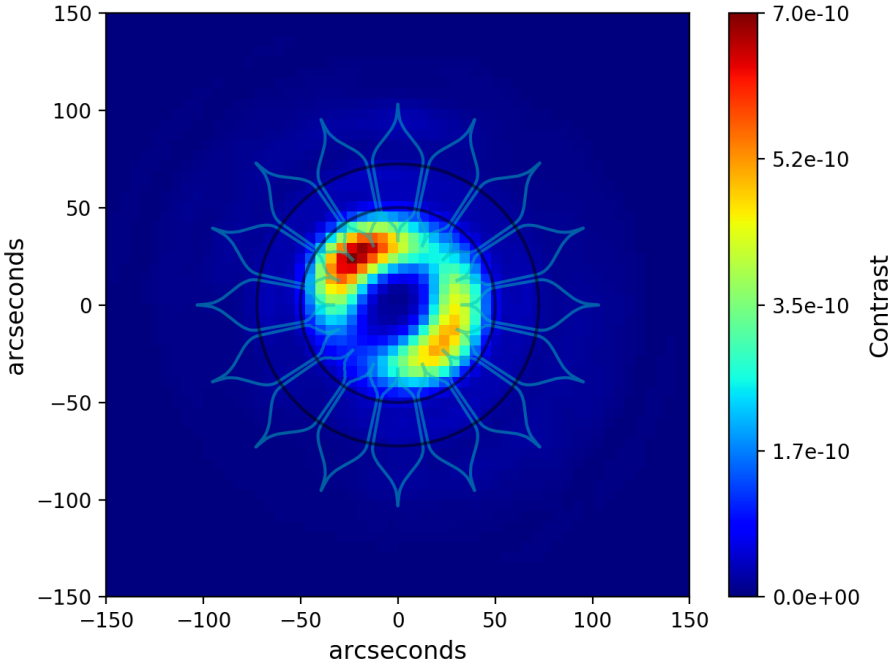

Figure 18: Contrast map for Run 1.

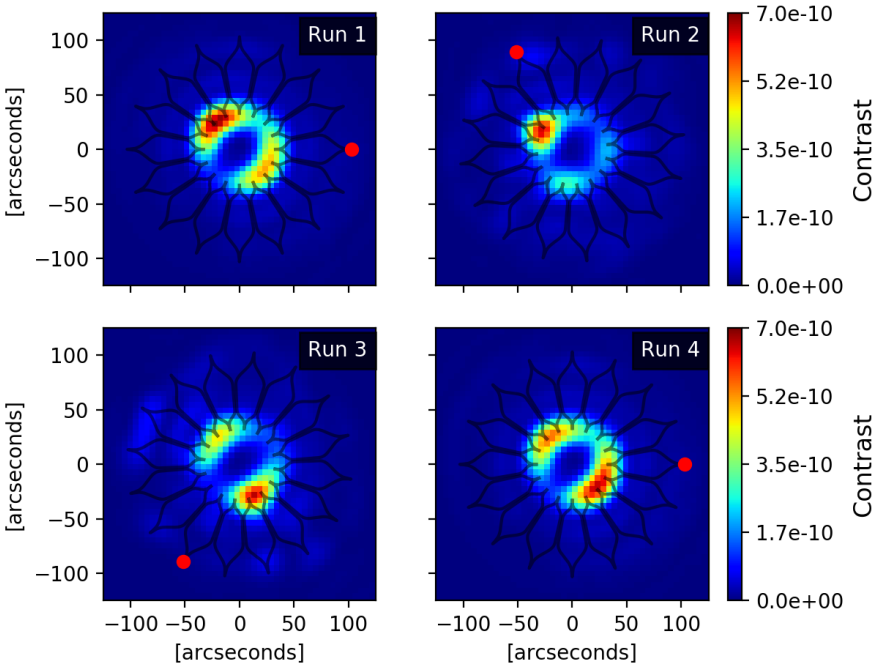

Figure 19: Contrast maps for the 4 observation runs in Table 3. The red dot marks the tip of the first petal of the mask.

The morphology of the inner lobes for Run 2 is quite different from the other runs and there are visible diffraction spots at the outer starshade ring. We attribute this difference to the mask being off-center relative to the through aperture of the mask holder while in this orientation. Seen in Figure 7b, there is a 75 mm diameter hole in the mask holder that serves as the fixed aperture through the baffle wall. When the starshade or calibration mask is in position, it should be aligned in the center of this aperture. Inspection of the mask at the Run 2 orientation showed that the starshade was up to 1 cm off-center in this aperture and that one side of the 50 mm diameter mask was slightly closer to the edge of the 75 mm diameter aperture. We believe that diffraction off the aperture interfered with the outer starshade and led to the bright spots seen around the outer mask. Curiously, this also reduced the central vector diffraction lobes; a phenomenon that needs further investigating and modeling to explain. Nonetheless, the results of Run 2 are still valid.

6 Model Comparison

The vector model combined with the scalar model is in good agreement with the experimental data and shows that the central lobes are due primarily to polarization effects from the 16 micron wide gaps at the innermost petal edges. Here, we provide a brief comparison of the experimental data to the scalar and vector diffraction models to better interpret our observations. Figure 20 shows images generated by the two models in comparison with the lab data. Slices parallel and orthogonal to the polarization vector direction are shown in Figure 21. The scalar model predicts a much lower (better) contrast than we observe, while the vector model shows rough agreement.

There is one free parameter, the effective mask edge thickness, in the vector model that is adjusted to find the best match to the experimental data. This occurred for a mask thickness of 0.9 μm, while the device layer of the mask is nominally 2 μm thick. We are currently pursuing this disagreement, a simple explanation being that the sides of the device layer are tapered such that the effective thickness is only 0.9 μm. Note that we have not subtracted the model from the data in the following analysis, but we are confident that the source of the bright lobes in the center of the data is due to polarization through the narrow slits, an effect that will be negligible at the flight scale, a point further discussed below.

7 Milestone Analysis

Our milestone is to achieve 10^{-10} contrast at the inner working angle of the starshade. Table 4, Figure 23, and Figure 24 show that we meet this requirement over a significant portion of the IWA annulus. The bright lobes from non-scalar diffraction at the base of the petals cause the contrast to rise above 10^{-10} over the remainder of the IWA annulus. Also presented in Table 4 is the fraction of the available search space through the open areas of the starshade mask that have contrast better than 10^{-10}. The following section details how these results were derived. Details of the calculations are given in Appendix A.

The contrast maps of Figure 18 and Figure 19 are the discrete contrast values calculated for individual camera pixels. A more meaningful contrast definition that ties directly to

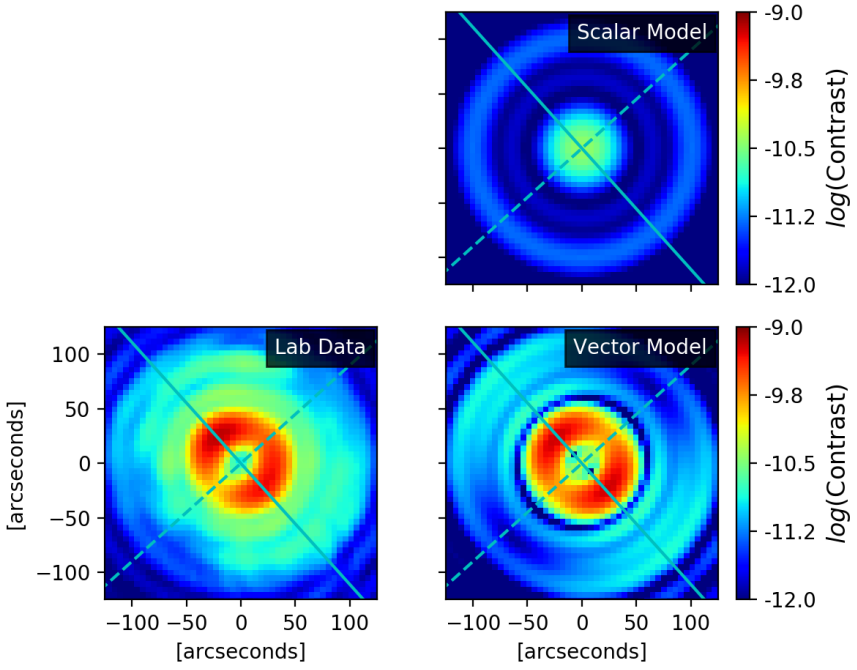

Figure 20: Contrast images from experimental data (lower left), the scalar diffraction model (upper right), and the vector diffraction model (lower right).

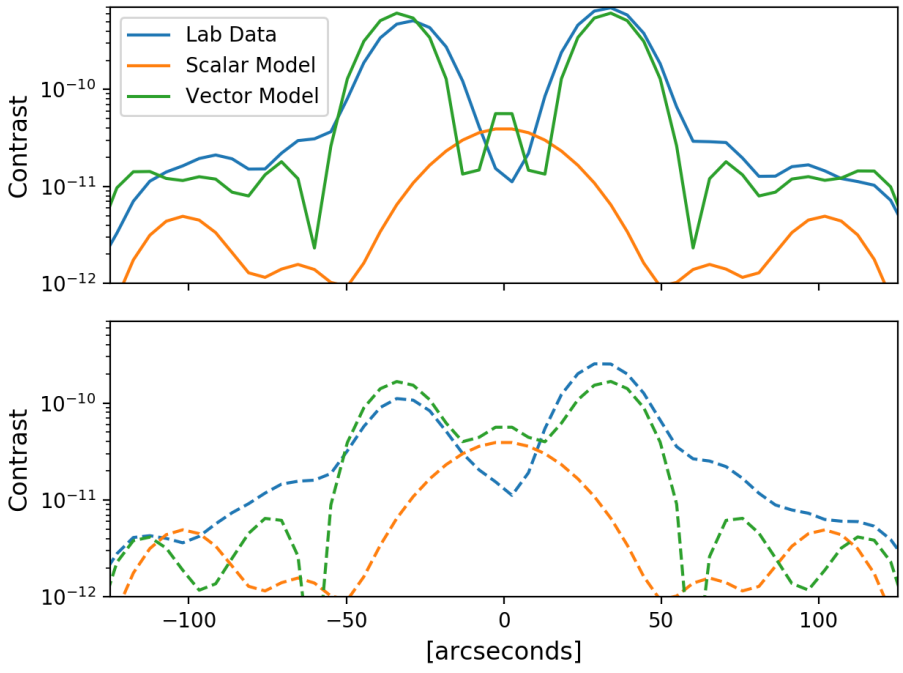

Figure 21: Slices across the contrast images in Figure 20. The top and bottom panels are slices along the solid and dashed lines, respectively, in Figure 20.

Observation Run	Fraction of IWA with Contrast $< 10^{-10}$	Fraction of Total Search Space
1	32.4 ± 7.9 %	88.4 ± 2.4 %
2	70.5 ± 8.2 %	94.9 ± 1.0 %
3	42.3 ± 7.8 %	88.6 ± 1.9 %
4	32.0 ± 5.7 %	88.1 ± 2.6 %
average	44%	90%

Table 4: For each observing run, we present the fraction of pixels at the IWA and over the total search area that have a contrast averaged over a λ/D aperture of $< 10^{-10} - 3\sigma$. The estimated systematic noise error is $\sigma = 2.3\%$.

the detection of planets is the average contrast within a λ/D wide photometric aperture. Referred to as the *aperture contrast*, for each pixel in the image, we average the contrast over a λ/D wide circle centered on that pixel. A pixel that has an aperture contrast above 10^{-10} does not meet the requirement of the milestone. Figure 22 shows the aperture contrast for the four observation runs with a mask applied to those pixels that exceed 10^{-10} - 3σ.

The loss of the masked pixels results in a diminished search space at the IWA, but quickly recovers to complete coverage just beyond the IWA. To calculate the fraction of search space available, we count the fraction of pixels within a 1 pixel wide annulus at a given radius that have an aperture contrast $< 10^{-10} - 3\sigma$ and divide by the total number of pixels in that annulus. In other words,

$$\text{Fraction} = \frac{\text{Number of pixels in annulus with aperture contrast} < 10^{-10} - 3\sigma}{\text{Total number of pixels in annulus}} \tag{9}$$

Defining which pixels constitute an annulus at a given radius is made difficult by the pixelization of the image. To more smoothly capture the fraction as a function of radius, we step radially in sub-pixel increments and grab all pixels whose center lies within the 1 pixel wide annulus centered on that radius. This is further complicated by the uncertainty in the plate scale of the image due to uncertainty in the camera's focal length. To account for these uncertainties, for each radius we calculate the fraction in 1 pixel wide annulus centered on three points: at the current radius and at ± the 1σ error in the focal length. The spread in the fraction and radii of the three points provide the uncertainties for that annulus. These values are then used to compute a weighted moving average of the fraction, with weights inversely proportional to the radial distance from the current evaluation radius. Figure 23 shows the fraction as a function of radius for each of the sub-pixel sampling points, along with the weighted average. The weighted averages for all observation runs are shown in Figure 24.

The value of the weighted average at the IWA is presented in Table 4. The quoted uncertainty is the standard deviation of fraction values in the IWA moving average bin. Also calculated in Table 4 is the fraction of the total search space, between the IWA and the outer working angle (the start of the outer apodization function), that meets the milestone.

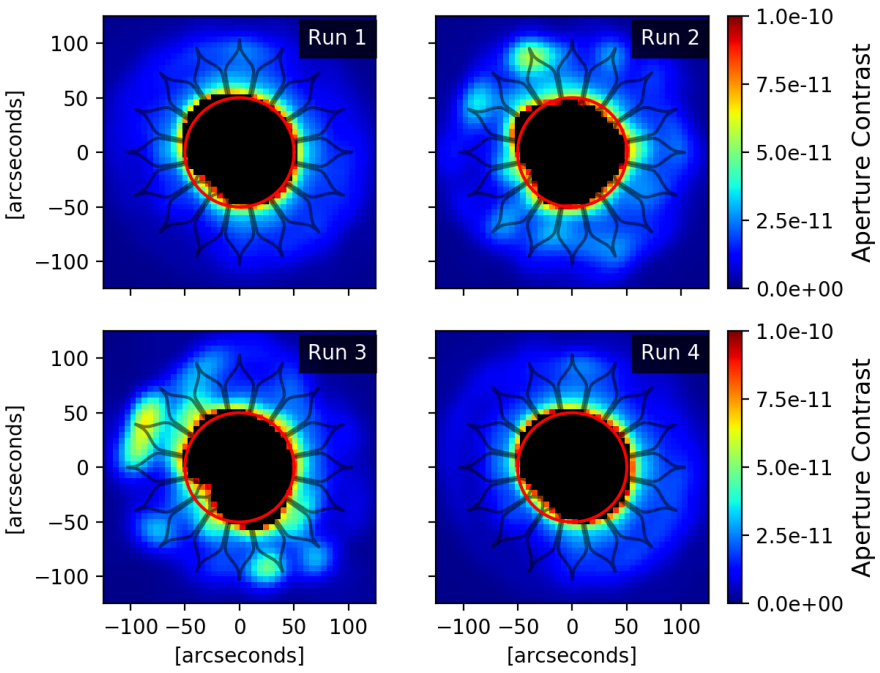

Figure 22: Contrast averaged in λ/D wide photometric aperture centered on each pixel. Black pixels are where the average contrast is greater than 3σ below 10^{-10}.

The uncertainty comes from propagating the uncertainty in the focal length to the location of the IWA and OWA.

In Figure 25 we plot the contrast averaged over a λ/D wide annulus as a function of radius. We will call this the *annulus contrast*. For each radial point, the raw contrast values for pixels that lie in the annulus centered on that point are averaged together. Note that this is different from averaging over the circular photometric aperture as was done for previous calculations and that this simulates the effect of rotating the starshade during an exposure to smear diffractive defects into a smooth annulus.

8 Discussion

Our primary milestone results are presented in Table 4 and Figure 24. Due to non-scalar diffraction lobes originating at the narrow valleys between starshade petals, the milestone is met between the lobes but not over the entire search space of the IWA. The annular contrast at the IWA is 1.15×10^{-10}, and the annular contrast is better than 10^{-10} for radii > 1.05 IWA. The vector-propagation lobes are a limitation that can be mitigated either by fabricating a thinner mask, which has proven to be elusive due to the susceptibility of the edge to damage, or by increasing the scale of the test to be hundreds of meters long, a proposition that would likely require a vacuum and greatly increase the cost and complexity of the tests.

The results of Figure 25 speak to a promising strength of starshades. The sources of instrument contrast are confined to the starshade, and the contrast improves as one looks at

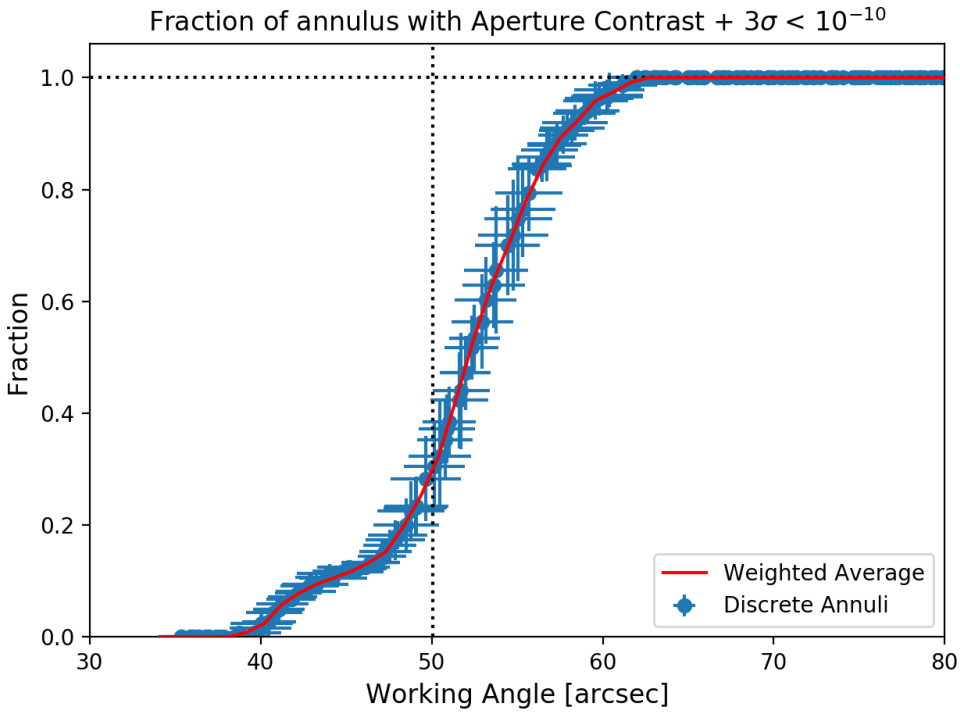

Figure 23: The fraction of pixels that meet the milestone aperture contrast within 3σ as a function of radial working angle for Run 1 (see Equation 9). The pixels are collected from a 1 pixel wide annulus centered on each incremental radius. The error bars are a result of error in the focal length leading to uncertainty in the angular position. The red line is the weighted average of the discrete annuli. The vertical line denotes the geometric IWA.

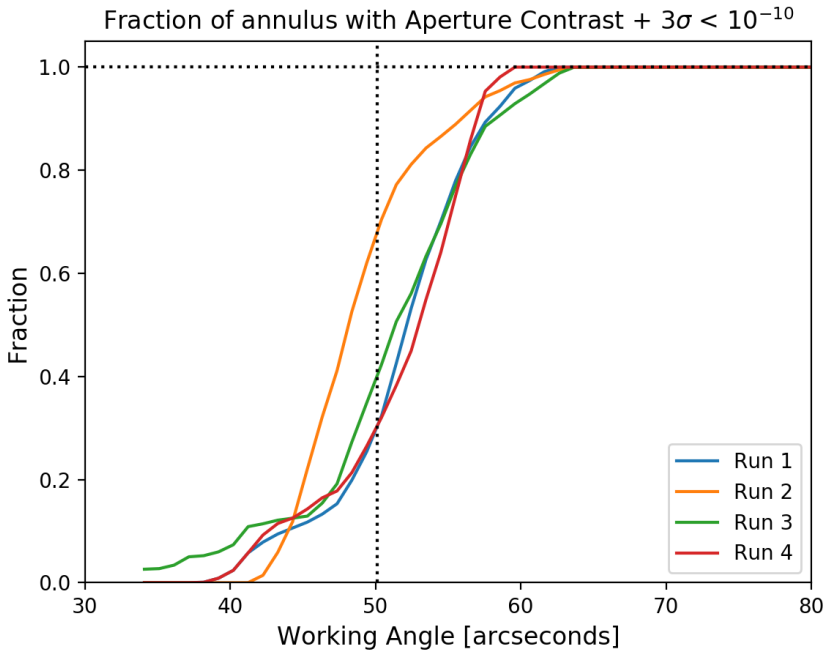

Figure 24: The weighted average fraction of pixels that meet the milestone contrast (as seen in Figure 23) for all observation runs.

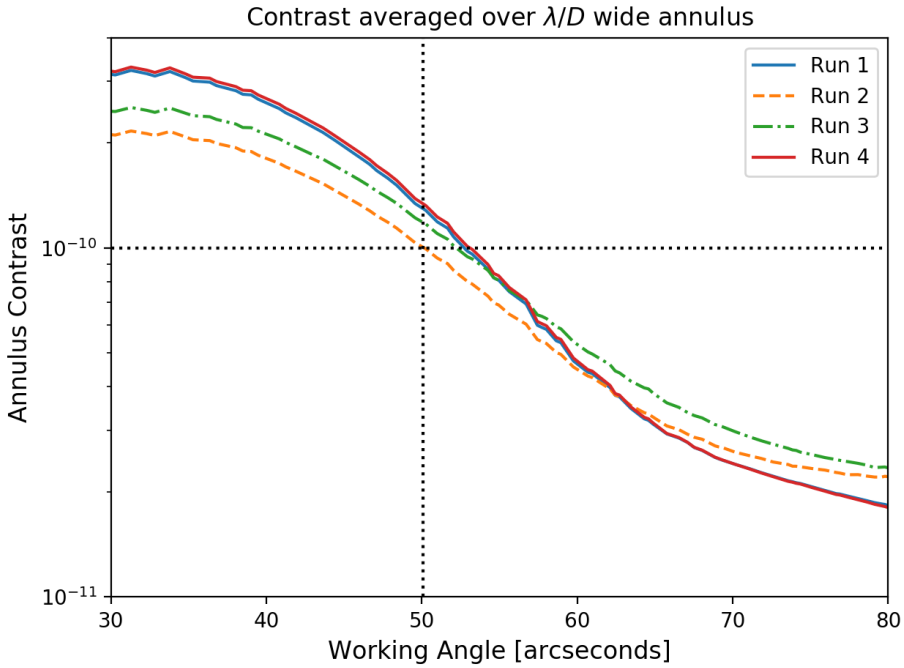

Figure 25: Contrast averaged over a λ/D wide annulus as a function of radial working angle for all observation runs.

radii beyond the starshade tips. Table 4 shows there is only a slight reduction in the fraction of total available search space (the fraction of available search space is underestimated due to the outer apodization function imposing an outer working angle limit that will not be present in flight). This tells us that although not optimal, the IWA and contrast can be achieved at the cost of a slightly larger, more distant starshade.

The contrast near the IWA is dominated by the bright lobes emanating from the inner valleys of the laboratory-scale starshade petals. The lobes are due to non-scalar diffraction effects resulting from light propagating through the narrow gaps that are only 20 wavelengths wide. Section 6 showed that scalar diffraction is not sufficient but that including the effects of non-scalar diffraction puts us close to agreement with the lab data. Attributing the regions of reduced contrast to non-scalar diffraction is further supported by the fact that the bright lobes maintain their position when the mask is viewed at other orientations and that they roughly align with the measured polarization vector. Data with the polarization vector at different orientations is shown in Appendix E.

While this is the dominant effect in the lab and is preventing us from achieving any higher contrast, we believe it will not be an issue for the space mission. Results from our vector diffraction model show that the polarization effects are confined to the edges of the petals, independent of gap width, effectively reducing the gaps by a fixed amount. The intensity of vector diffraction vs scalar diffraction is then a ratio of the perimeter of the starshade to its surface area, which scales as $1/r^2$. Thus for a space mission with a $1000\times$ larger radius, the effect of vector diffraction should be $10^6\times$ smaller.

The aim of this milestone is to help advance the optical technology of starshades to TRL 5, with a focus on model validation at flight-like contrast levels and flight-like Fresnel numbers. Milestone 1A represents the initial step in the demonstration of TRL 5 by utilizing a medium fidelity system to demonstrate overall performance in critical areas in a simulated operational environment. The construction of this testbed and the ability to test at a flight-like Fresnel number are meant to provide a hi-fidelity simulated operational environment. Achieving 10^{-10} contrast demonstrates that we are capable of designing a starshade that can provide the starlight suppression necessary to achieve our scientific goals. Future efforts in validating the model predictions of sensitivity to shape errors will ensure that the error budgeting process leads to shape requirements that will meet flight contrast requirements.

9 Conclusion

The data presented in this report represent the best performance of a flight-like starshade to date. With a starshade of Fresnel number = 13, in monochromatic light, we achieved an average contrast at the IWA of 1.15×10^{-10}. At the IWA, $\sim$44% of the search space was below 1×10^{-10} while the rest was attributed to non-scalar diffraction related to the microscopic openings at the inter-petal valleys of the laboratory-scale mask, an effect germane to the scale of the test article. Despite the contamination, the annular contrast is below 1×10^{-10} immediately outside the IWA and beyond, with a contrast floor of $\sim 2 \times 10^{-11}$. The floor, we believe, is largely caused by Rayleigh scatter by air molecules, as discussed in Appendix D.

Successful completion of this milestone verifies we can design a starshade capable of pro-

ducing scientifically useful contrast levels and is the first foundational block in demonstrating that starshade technology is at TRL 5. The next experiment at the Princeton Testbed will demonstrate 10^{-10} contrast in 4 wavelengths across a 10% bandpass. Following this will be a sensitivity study measuring contrast of intentionally induced shape errors to validate the optical models to 25% agreement. Completion of these milestones will leave starshade optical technology at TRL 5 and well poised for further advancement.

Acknowledgments

This work was performed in part at the Jet Propulsion Laboratory, California Institute of Technology under a contract with the National Aeronautics and Space Administration. Starshade masks were manufactured using the facilities at the Microdevices Lab at JPL. This project made use of the facilities at the Princeton Micro/Nano Fabrication Laboratory. The authors would like to thank Yunjong Kim (now at the Korean Astronomy and Space Science Institute) for his previous efforts with the testbed. The authors would also like to thank Kendra Short, Stefan Martin, Michael Bottom, and Brendan Crill for reviewing this work and for providing helpful comments.

References

[1] P. Willems, "Starshade to TRL5 (S5) Technology Development Plan," *Jet Propulsion Laboratory Publications* , 2018.

[2] B. Gaudi, S. Seager, B. Mennesson, and et al., "The Habitable Exoplanet Observatory (HabEx) Mission Concept Study Interim Report," *ArXiv e-prints* **1809.09674**, 2018.

[3] S. Seager, J. Kasdin, and Starshade Rendezvous Probe Team, "Starshade Rendezvous Mission Probe Concept," in *American Astronomical Society Meeting Abstracts #231*, **231**, p. 121.09, Jan. 2018.

[4] D. B. Leviton, W. C. Cash, B. Gleason, M. J. Kaiser, S. A. Levine, A. S. Lo, E. Schindhelm, and A. F. Shipley, "White-light demonstration of one hundred parts per billion irradiance suppression in air by new starshade occulters," *Proc. SPIE* **6687**, p. 12, 2007.

[5] R. Samuele, T. Glassman, A. M. J. Johnson, R. Varshneya, and A. Shipley, "Starlight suppression from the starshade testbed at ngas," *Proc. SPIE* **7440**, p. 9, 2009.

[6] R. Samuele, R. Varshneya, T. P. Johnson, A. M. F. Johnson, and T. Glassman, "Progress at the starshade testbed at northrop grumman aerospace systems: comparisons with computer simulations," *Proc. SPIE* **7731**, p. 12, 2010.

[7] T. Glassman, S. Casement, S. Warwick, and M. Novicki, "Measurements of high-contrast starshade performance," *Proc. SPIE* **9143**, p. 13, 2014.

[8] T. Glassman, M. Novicki, M. Richards, D. Smith, S. Warwick, K. Patterson, and A. Harness, "2012 TDEM: Demonstration of Starshade Starlight-Suppression Performance

in the Field. Final Report," *Jet Propulsion Laboratory Publications* **JPL Document 1469885**, Sep 2012.

[9] A. Harness, S. Warwick, A. Shipley, and W. Cash, "Ground-based testing and demonstrations of starshades," *Proc. SPIE* **9904**, p. 14, 2016.

[10] A. Harness, W. Cash, and S. Warwick, "High contrast observations of bright stars with a starshade," *Experimental Astronomy* **44**, pp. 209–237, Nov. 2017.

[11] E. Cady, K. Balasubramanian, M. Carr, M. Dickie, P. Echternach, T. Groff, N. J. Kasdin, C. Laftchiev, M. McElwain, D. Sirbu, R. Vanderbei, and V. White, "Progress on the occulter experiment at princeton," *Proc. SPIE* **7440**, p. 10, 2009.

[12] D. Sirbu, E. J. Cady, N. J. Kasdin, R. J. Vanderbei, J. Lu, and E. Kao, "Optical verification of occulter-based high contrast imaging," *Proc. SPIE* **8151**, p. 12, 2011.

[13] M. Galvin, Y. Kim, N. J. Kasdin, D. Sirbu, R. Vanderbei, D. Echeverri, G. Sagolla, A. Rousing, K. Balasubramanian, D. Ryan, S. Shaklan, and D. Lisman, "Design and construction of a 76m long-travel laser enclosure for a space occulter testbed," *Proc. SPIE* **9912**, p. 18, 2016.

[14] Y. Kim, D. Sirbu, M. Galvin, N. J. Kasdin, and R. J. Vanderbei, "Experimental study of starshade at flight fresnel numbers in the laboratory," *Proc. SPIE* **9904**, p. 11, 2016.

[15] H. G. Berry, G. Gabrielse, and A. E. Livingston, "Measurement of the Stokes parameters of light," *Applied Optics* **16**, pp. 3200–3205, Dec. 1977.

[16] R. J. Vanderbei, E. Cady, and N. J. Kasdin, "Optimal Occulter Design for Finding Extrasolar Planets," *ApJ* **665**, pp. 794–798, Aug. 2007.

[17] K. Balasubramanian, D. Wilson, V. White, *et al.*, "High contrast internal and external coronagraph masks produced by various techniques," *Proc. SPIE* **8864**, p. 9, 2013.

[18] K. Balasubramanian, A. J. E. Riggs, E. Cady, *et al.*, "Fabrication of coronagraph masks and laboratory scale star-shade masks: characteristics, defects, and performance," *Proc. SPIE* **10400**, p. 16, 2017.

[19] W. Cash, "Analytic Modeling of Starshades," *ApJ* **738**, p. 76, Sept. 2011.

[20] E. Cady, "Boundary diffraction wave integrals for diffraction modeling of external occulters," *Optics Express* **20**, p. 15196, July 2012.

[21] A. Harness, S. Shaklan, W. Cash, and P. Dumont, "Advances in edge diffraction algorithms," *J. Opt. Soc. Am. A* **35**, pp. 275–285, Feb 2018.

[22] T. Glassman, A. Johnson, A. Lo, D. Dailey, H. Shelton, and J. Vogrin, "Error analysis on the nwo starshade," *Proc. SPIE* **7731**, p. 18, 2010.

[23] A. Harness, S. Shaklan, P. Dumont, Y. Kim, and N. J. Kasdin, "Modeling and performance predictions for the princeton starshade testbed," *Proc. SPIE* **10400**, p. 20, 2017.

[24] A. Harness, N. J. Kasdin, S. Shaklan, P. Dumont, and K. Balasubramanian, "Modeling non-scalar diffraction in the princeton starshade testbed," *Proc. SPIE* **10698**, p. 17, 2018.

[25] A. F. Oskooi, D. Roundy, M. Ibanescu, P. Bermel, J. Joannopoulos, and S. G. Johnson, "Meep: A flexible free-software package for electromagnetic simulations by the fdtd method," *Computer Physics Communications* **181**(3), pp. 687 – 702, 2010.

Appendix A: Contrast Definition

Contrast is defined as the amount of light within a resolution element of a telescope (at the image plane), divided by the peak brightness of the main light source as measured by that telescope when there is no starshade in place. The contrast is therefore a function of the telescope and the background light distribution. Contrast is a useful definition when talking about detectability of astronomical targets as it describes the noise contribution from residual starlight at the location of the object of interest. In practice, the ability to subtract a uniform or smoothly varying background enables the detection of a planet at a lower brightness than the instrument contrast. A proposed method to ensure a smoothly varying background is to spin the starshade during the observation and smear any localized defects into an annulus extending no further than the tip of the starshade. A simple method to extract the planet's signal from an image is to draw a photometric aperture around the planet and count the total flux in that aperture. In our milestone analysis, for each pixel in the image, we compute the average contrast in a photometric aperture of width λ/D centered on that pixel.

Free space propagation is not possible in the confinements of the lab, thus we use a circular calibration mask to measure the unocculted brightness and convert to a free space brightness through modeling. In the following definitions, the subscript of a symbol will denote the observation mode, with m denoting measurements made when the starshade *mask* is in place (also called "science" observations) and u denoting *unocculted* measurements when the calibration mask is in place (also called "calibration" observations).

We define the contrast at pixel i as

$$\begin{aligned} C^i &= \frac{\Gamma^i_m}{\Gamma^0_{\text{free space}}} \\ &= \frac{\Gamma^i_m}{\gamma A^2 \Gamma^0_u} , \end{aligned} \tag{10}$$

which is a theoretical construct specifying the reduction in brightness the starshade mask provides, relative to the on-axis unocculted source. The peak value of the apodization function (A^2) in the denominator accounts for the fraction of light that is blocked by the

Symbol	Description
C^i	Contrast at pixel i
Γ^i	Transfer function mapping to pixel i
γ	Ratio of PSF peak after propagation through free space to that of the calibration mask
A	Peak value of apodization function
s^i	Counts collected in pixel i during exposure of length t [ct]
P	Laser power [W]
ν	Neutral density filter transmission
ε	Transmission through atmosphere
τ	Throughput of camera optics
D	Aperture diameter [mm]
Q	Quantum efficiency of detector [e^-/ph]
E	Photon energy [J/ph]
G	Camera inverse-gain [e^-/ct]
t	Exposure time [s]
m	Denotes *mask/science* measurement
u	Denotes *unocculted/calibration* measurement

Table 5: List of variables used in contrast definition

radial struts supporting the inner starshade. The value γ is the ratio of the peak of the PSF after propagation through free space to that of after propagation through the circular calibration mask, and relates the contrast measured in the lab to that expected from a free-floating starshade. More details on this conversion can be found in Section 4.6

The transfer function is tied to a measurement through the equation:

$$s_x^i = \left(\frac{P\nu\varepsilon Q\tau t\Gamma^i}{EG}\right)_x, \tag{11}$$

where $x \in \{m, u\}$. We drop the superscript on s_u and assume it is on-axis. We assume there is no ND filter during starshade measurements ($\nu_m = 1, \nu_u \equiv \nu$) and that the photon energy, camera gain, and camera throughput do not change between observation modes. Substituting Equation 11 into Equation 10, we rewrite the contrast as

$$C^i = \left(\frac{\nu s_m^i t_u}{\gamma A^2 s_u t_m}\right)\left(\frac{P_u\varepsilon_u Q_u}{P_m\varepsilon_m Q_m}\right). \tag{12}$$

We assume that values in the right parentheses have the same mean between observation modes, but whose true value during a given observation is distributed normally around the mean with variance σ^2. In other words, $P_u = P_m \equiv P$, $\sigma_{P_u}^2 = \sigma_{P_m}^2 \equiv \sigma_P^2$, and similarly for ε, Q. This simplifies the contrast definition to

$$C^i = \frac{\nu s_m^i t_u}{\gamma A^2 s_u t_m}. \tag{13}$$

For each pixel, we calculate the average contrast over n pixels that lie within a λ/D wide photometric aperture at that pixel:

$$\begin{aligned} C &= \frac{1}{n}\sum_i^n C^i \\ &= \frac{1}{n}\frac{\nu t_u}{\gamma A^2 s_u t_m}\sum_i^n s_m^i \\ &\equiv \alpha \sum_i^n s_m^i \end{aligned} \tag{14}$$

Assuming independent measurement errors, the error in the average contrast is propagated to

$$\frac{\sigma_C^2}{C^2} = \frac{\sigma_\alpha^2}{\alpha^2} + \frac{\sum_i^n \sigma_{s_m^i}^2}{(\sum_i^n s_m^i)^2} \tag{15}$$

The uncertainty in the science images are estimated in Section 4.1.2. The error wrapped into the constant α is constant across exposures and is given by

$$\frac{\sigma_\alpha^2}{\alpha^2} = \frac{\sigma_{s_u}^2}{s_u^2} + \frac{\sigma_\gamma^2}{\gamma^2} + \frac{\sigma_\nu^2}{\nu^2} + 2\frac{\sigma_\varepsilon^2}{\varepsilon^2} + 2\frac{\sigma_P^2}{P^2} + 2\frac{\sigma_Q^2}{Q^2}. \tag{16}$$

We estimate the values of these uncertainties in Section 4.

Appendix B: Data Collection Procedures

The following summarizes the procedure for conducting a contrast observation run.

1. Install mask and let atmosphere in tube settle for > 3 days
2. Cool camera down to -90°C
3. Turn *on* laser
4. Move mask changer to calibration mask
5. Move ND filter *in*
6. Switch optics to pupil imaging mode
7. Align diffraction pattern in center of aperture
8. Switch optics to far field imaging mode
9. Take series of unocculted contrast images (7 s exposure time)
10. Move mask changer to starshade mask
11. Move ND filter *out*

12. Switch optics to pupil imaging mode
13. Align diffraction pattern in center of aperture
14. Switch optics to far field imaging mode
15. Take series of mask contrast images (1200 s exposure time)
16. Turn *off* laser
17. Take series of background unocculted images (7 s exposure time)
18. Take series of background mask images (1200 s exposure time)

Appendix C: Experiment Suppression Data

For completeness, Figure 26 includes an image of the pupil, in units of discrete suppression. Suppression is defined as the total amount of light incident on an aperture when the starshade is in place, divided by the total amount of light incident on the same aperture when there is no starshade in place. Using the suppression definition outlined in Ref. 23, the *total suppression* achieved is 6.6×10^{-9}.

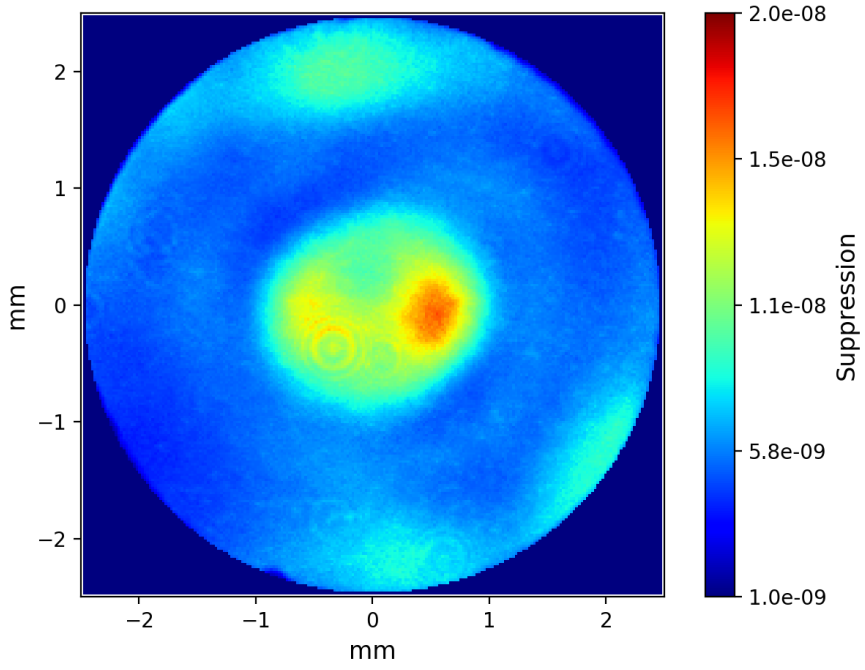

Figure 26: Suppression map for Run 1.

Appendix D: Rayleigh Scattering Model

We have begun analysis of the expected light levels in the testbed images due to Rayleigh scattering by air molecules. This analysis uses a purely geometrical optics model to determine the pattern of illumination within the testbed chamber, and then applies the Rayleigh scattering formula to the known atmospheric densities of molecular nitrogen and oxygen, which together account for $\sim$ 99% of the scattering in clean air. (The method can also model the additional scattering due to fine airborne dust, but such dust does not appear to be necessary to explain the Rayleigh scattering features in the data.) The amount of light scattered into the camera aperture from a given direction determines the brightness of the scattered light in that region of the contrast image.

Figure 27 shows the contrast image on a logarithmic scale, along with the image produced by the Rayleigh scattering model. These images are zoomed out relative to the others in this report to show the light levels well outside the outer working angle of the mask, where diffraction theory predicts they should be extremely low. The scattering model reproduces well the 'spokes' seen in the data, although it shows dark gaps where the struts in the masks cast shadows into the testbed's camera chamber that are not seen in the data. This is due to the geometrical optics assumed by the Rayleigh scattering model. A better model of the illumination pattern that accounts for diffraction of the light projecting through the mask is expected to 'fill in' these gaps.

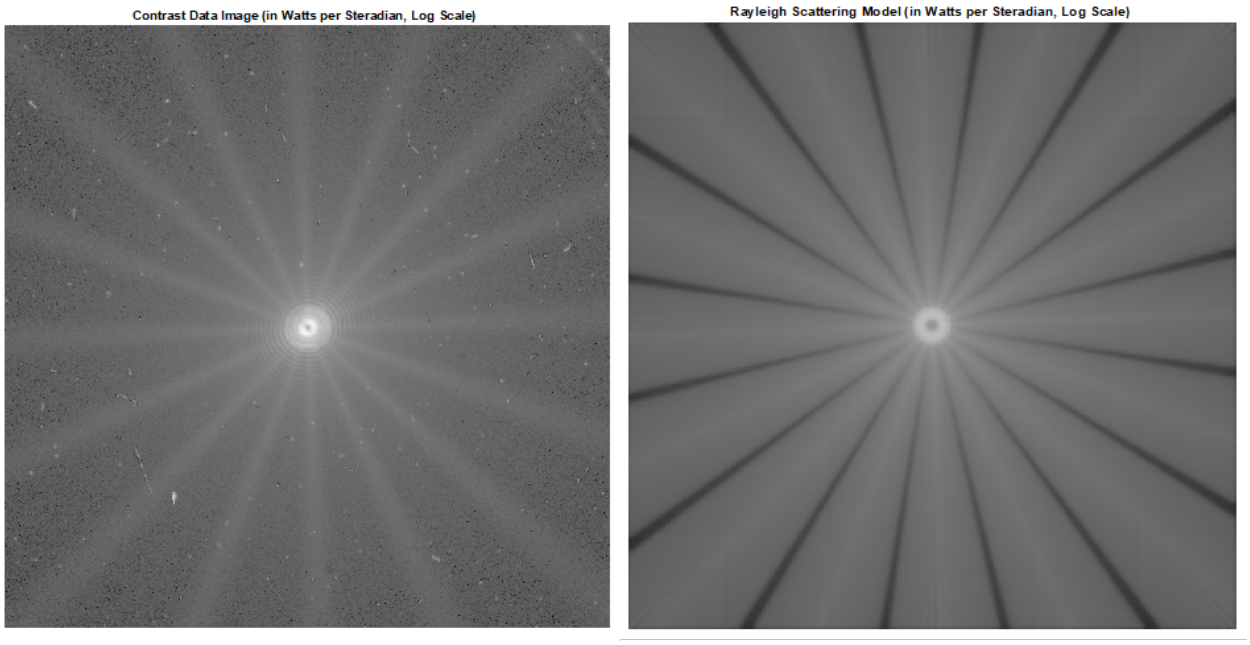

Figure 27: Left: the contrast image from Run 1, zoomed out to show Rayleigh scattered light at large angles. Right: the prediction of the Rayleigh scattering model. The FOV is 52.3' x 52.3'.

Figure 28 shows a plot of the contrast along a line through the contrast image of run 1, along with the prediction of the Rayleigh scattering model. The line plot is roughly along

one of the bright 'spokes' in Figure 27. The Rayleigh scattered contrast averaged over a λ/D-wide annulus at the inner working angle is $\sim 1.2 \times 10^{-11}$.

The Rayleigh scattering model also calculates total amount of scattered light entering the camera aperture when the camera collects a pupil image, to determine the contribution of Rayleigh scattering to the overall suppression. The model only includes light that passes through the camera's field stop when making this calculation, as light that enters the aperture at steeper angles does not reach the detector. For Run 1, the suppression due to Rayleigh scattering is calculated to be $\sim 5.5 \times 10^{-9}$. This is close to the $\sim 6.6 \times 10^{-9}$ suppression actually measured, suggesting that although Rayleigh scattering is a relatively small contribution to the contrast at the inner working angle, it is responsible for most of the light entering the aperture.

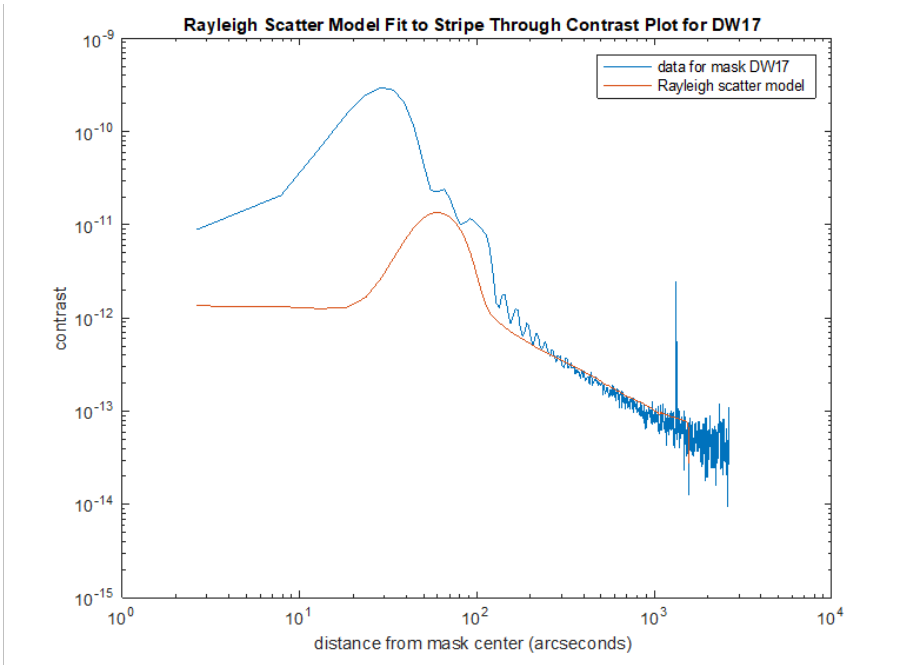

Figure 28: Measured contrast profile and predicted Rayleigh scattering profile for Run 1.

Appendix E: Effects of Varying Polarization State

Figure 29 shows the contrast images of various polarization states to further support our claim that the bright lobes at the inner valleys of the starshade are due to polarization. A linear polarizer is placed on a motorized rotation stage between the collimated terminus of the fiber and the spatial filter, and the polarization axis rotated from 0° to 180°, relative to the camera's vertical axis. The orientation of the bright lobes clearly track with the axis of polarization. The lobe brightness varies with orientation: we attribute this to non-uniform illumination of the 100 μm diameter pinhole as the polarizer is rotated.

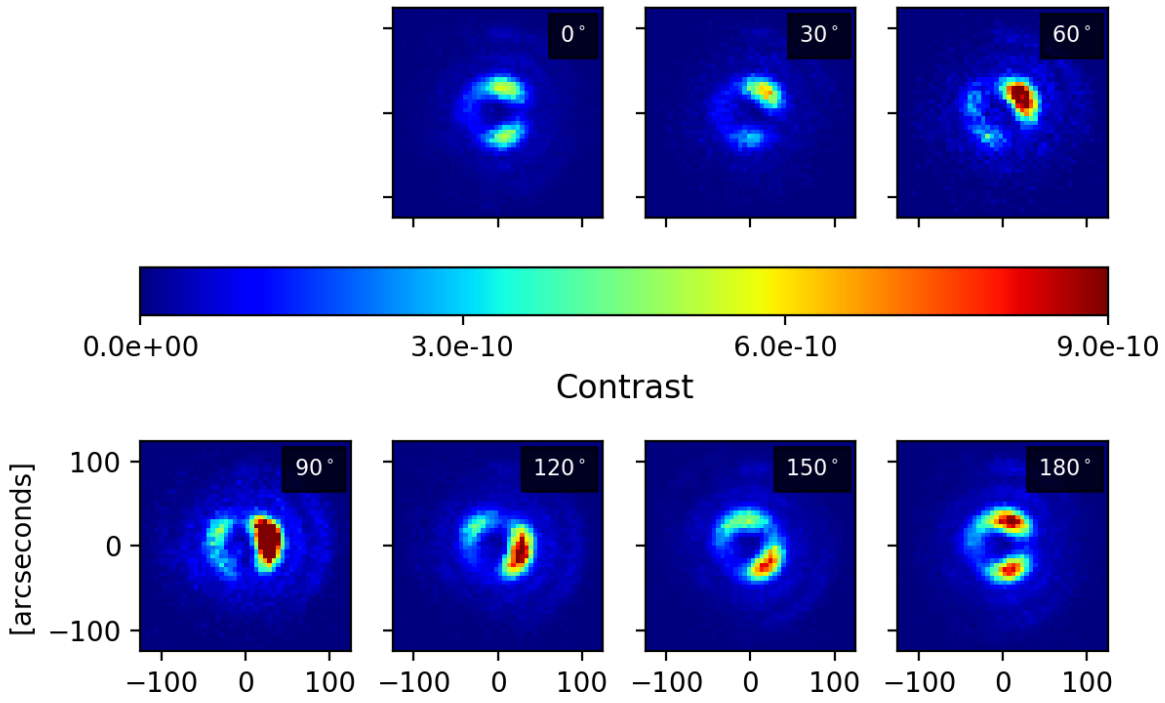

Figure 29: Contrast images with a linear polarizer in front of the light source. The angle of the linear polarizer's polarization axis is relative to the camera's vertical axis.